FABRICATION AND EVALUATION OF GERMANIUM DOPED CESIUM TIN TRIIODIDE PEROVSKITE SOLAR CELLS

MARION KERUBO MOGUSU

A Thesis Submitted to the Graduate School in Partial Fulfilment of the Requirement for Master of Science Degree in Physics of Egerton University

EGERTON UNIVERSITY

SEPTEMBER, 2025

DECLARATION AND RECOMMENDATION

Declaration

This thesis is my original work and has not been presented in this university or any another for the award of a degree

Signature…..... Date: 20/08/2025

Marion Kerubo Mogusu

SM13/04102/22

Recommendation

This thesis has been submitted with our approval as university supervisors

Signature . Date: 20/08/ 2025

Dr Duke Oeba, PhD

Department of Physics

Egerton University

Signature……..... ..... Date: 20/08/2025

Dr Cliff Orori Mosiori, PhD

Department of Mathematics and Physics

Technical University of Mombasa

DEDICATION

I would like to dedicate this thesis to all my family members. Their commitment, support, encouragement, and sacrifices were the forces driving my academic journey. In particular, my parents for their prayers, endless love, sacrifices and belief in my work and to my siblings, for always being present when I needed them and for their constant motivation.

ACKNOWLEDGEMENTS

I would like to thank God the Almighty for the gift of life, for continuing to guide and protect me through this journey. I gratefully acknowledge Egerton University for the providence of the necessary resources as well as facilities to support this work. I also appreciate the support of UNESCO-TWAS for financial assistance which made this research duly possible. I thank the University of Michigan, USA, for allowing the use of their Rigaku Ultima IV X-ray diffractometer and FEI Nova 200 NanoLab SEM for structural and morphological characterization, respectively. I am eternally grateful to my supervisors, Dr. Duke Oeba and Dr Cliff Mosiori, for their critical guidance, insightful feedback, and unwavering support throughout this research journey. Their mentorship has played a crucial role in shaping my academic and professional growth.

I accord my heartfelt gratitude to the members of my family, my father, Mr. Tom Mogusu, my mother, Ms. Jane Odanga, my brother, Antony Onkeo and my sisters, Lillian Kemunto and Winnie Moraa for their prayers, financial and moral support. I also wish to acknowledge with profound appreciation the moral and emotional support of my friends, I deeply apologize to them all for every moment that my work put me away from them. Lastly, a special thanks goes to all my colleagues from the Physics department as well as the staff, you inspired and supported me in all the ways you could throughout this entire process. I am grateful and appreciative of you all.

ABSTRACT

In the ever-evolving landscape of renewable energy technologies, perovskite solar cells (PSCs) have emerged as an alternative for efficient and affordable photovoltaics (PVs). The quest for sustainable energy sources, coupled with the need to eliminate toxic lead content has called for research in inorganic, cost effective and stable lead-free PSCs. In this work, tin (IV) oxide (SnO_2) electron transport layer (ETL) and germanium doped cesium tin triiodide ($CsSnI_3$-Ge) perovskite layer, incorporated with a 5mole% Ge concentration were deposited via thermal evaporation and spin coating methods respectively. In the deposition of SnO_2 films, the thickness was varied, and $CsSnI_3$-Ge films were deposited under different spin coating speeds. Optical measurements were done using the ultraviolet visible (UV-Vis) spectrophotometer while structural and morphological measurements for the perovskite layers were performed using an X-ray diffraction (XRD) and scanning electron microscope (SEM) machines respectively. Our findings show that optical properties for the 30 nm thickness ETL displayed a higher transmittance of approximately 80%, and the band gap values ranged from 3.02 eV to 3.34 eV. The $CsSnI_3$-Ge layer deposited at a spin coating speed of 4000 rpm displayed the highest absorbance of approximately 0.77 a.u attaining a band gap value in the range of 2.85 eV to 3.35 eV which was higher than the ideal value of ~1.5 eV. Structural analysis on $CsSnI_3$-Ge films displayed a consistent orthorhombic structure across all samples. The crystallite sizes were nearly identical, as was seen in SEM images. Generally, the perovskite film synthesized by spin coating speed of 4000 revolutions per minute (rpm) displayed higher absorbance, higher crystallinity and a relatively uniform film morphology making it the optimal layer for fabrication. Three perovskite structures of fluorine doped tin (IV) oxide (FTO)/SnO_2/$CsSnI_3$-Ge/copper (I) oxide (Cu_2O)/graphite were fabricated and their current density-voltage (J-V) characteristics investigated using a solar cell simulator. From the results, the best performing cell attained a power conversion efficiency (PCE) of 2.458% with an open circuit voltage (V_{oc}) of 0.7056 V, a short circuit current density (J_{sc}) of 8.868 $mA.cm^{-2}$ and a fill factor (FF) of 39.27%. This output was less than expected but agrees with that of several Sn based PSCs. An optimal annealing temperature has been recommended for the SnO_2 ETL for band gap control as well as an all-vacuum environment for the synthesis of Sn based perovskites. Alternative synthesis routes for Ge doping should also be explored and interface/surface passivation strategies should be considered for an improved V_{oc}. Additionally, hall effect measurement is recommended to determine the charge carrier concentration. This study will help contribute to advancements in renewable energy technologies, research and promotion of sustainable energy solutions.

TABLE OF CONTENTS

LIST OF FIGURES

LIST OF ABBREVIATIONS & ACRONYMS

CIGS	Copper indium gallium selenide
CNTs	Carbon nano tubes
CVD	Chemical vapor deposition
DMF	Dimethylformamide
DMSO	Dimethylsulfoxide
DSSCs	Dye sensitized solar cells
ETL	Electron transport layer
ETM	Electron transport material
FA	Formamidinium
FF	Fill factor
FTO	Fluorine doped tin oxide
HTL	Hole transport layer
HTM	Hole transport material
IEC	International Electrotechnical Commission
ITO	Indium tin oxide
MA	Methylammonium
Mo	Molybdenum
n-i-p	Negative-intrinsic-positive
OSCs	Organic solar cells
PCE	Power conversion efficiency
PEDOT: PSS	Poly(3,4-ethylenedioxythiophene): poly (styrenesulfonate)
p-i-n	Positive-intrinsic-negative
ppm	Parts per million
PSCs	Perovskite solar cells
PTAA	Poly[bis(4-phenyl) (2,4,6-trimethylphenyl) amine]
PV	Photovoltaic
RH	Relative humidity
ROHS	Restriction of hazardous substances
Rpm	Revolutions per minute
R_{series}	Series resistance
R_{shunt}	Shunt resistance
SCs	Solar cells
SDGs	Sustainable development goals

SEM	Scanning electron microscope
Spiro-OmeTAD	Spiro [flourene-9,9'-xanthene]-2,2',7,7'-tetramine
SRH	Shockley-Read-Hall
TCO	Transparent conductive oxide
UV-Vis	Ultraviolet visible spectroscopy
XRD	X-ray diffraction

LIST OF SYMBOLS

Å	Angstrom unit
Ag	Silver
Au	Gold
Bi	Bismuth
Br	Bromine
Bα	Black cubic phase
Bβ	Black tetragonal phase
Bγ	Black orthorhombic phase
$CaTiO_3$	Calcium titanate
CdTe	Cadmium telluride
$CH_3NH_3PbI_3$	Methylammonium lead iodide
Cs	Cesium
CsI	Cesium (II) iodide
c-Si	Crystalline silicon
$CsSnGeI_3$	Cesium tin germanium triiodide
$CsSnI_3$	Cesium tin triiodide
$CsSnI_3$-Ge	Germanium doped cesium tin triiodide
Cs_6SnI_6	Cesium hexaiodostannate (IV)
CuI	Copper (I) iodide
Cu $(OAc)_2$	Acetic acid
Cu_2O	Cuprous oxide
E_g	Band gap
$FASnI_3$	Formamidinium tin triiodide
GaAs	Gallium arsenide
Ge	Germanium
GeI_2	Germanium (II) iodide
h	Planck's constant
I	Iodine
I_{mp}	Current at maximum power
I_{sc}	Short circuit current density
$MASnI_3$	Methylammonium tin triiodide
P_{mp}	Maximum power point
P_{sun}	Power of sunlight

Pb	Lead
Pb^{2+}	Lead cation
PbI_2	Lead (II) iodide
Rb	Rubidium
Sb	Antimony
Sn	Tin
Sn^{2+}	Tin cation
SnI_2	Tin (II) iodide
SnI_4	Tin (IV) iodide
SnF_2	Tin (II) floride
SnO_2	Tin (IV) oxide
Ti	Titanium
TiO_2	Titanium dioxide
$V^{-1}s^{-1}$	Reciprocal of volt seconds
V_{mp}	Voltage at maximum power
V_{oc}	Open circuit voltage
ZnO	Zinc oxide
η	Power conversion efficiency
ζ	Carrier lifetime
α	Absorption coeffient
λ	Wavelength

CHAPTER ONE
INTRODUCTION

1.1 Background Information

The search for a source of energy that is commercially viable and environmentally sustainable has been ongoing for many years. The current global demand for power is at 16 TW and is estimated to increase beyond 30 TW by 2050 (Roy *et al*., 2020). Therefore, researchers are working tirelessly to help develop a power generation system that will meet this global demand. In most cases, non-renewable resources are used in energy production. This leads to the depletion of fossil fuels at a faster rate and causes a tone of environmental problems like pollution and climate change (Sathiyan *et al*., 2022). Burning of fossil fuels cannot cover the hike in power demand. Therefore, renewable energy sources offer a friendly alternative source for power generation (Abas *et al*., 2015). Nuclear, tidal, geothermal, hydropower, wind and solar energies are some of the preferred renewable energy sources.

Nuclear energy produces a significant amount of power and has low greenhouse gas emissions. However, it comes with concerns about its radioactive waste disposal, potential accidents like harmful radiation leakages, and high capital costs for construction and decommissioning nuclear plants (Iqbal *et al*., 2021). The advantage of tidal energy is the utilization of ocean tides' kinetic energy to generate electricity. However, its feasibility is limited to regions which experience strong tidal flows, which also restricts its global applicability. The construction and maintenance of tidal energy infrastructure can also have serious environmental impacts on marine ecosystems (Roberts *et al*., 2016). Hydropower, or hydroelectric power on the other hand, is produced from the utilization of the energy generated from flowing water. One of the factors that affect its power generation is adequate water supply and can be influenced by droughts and changing precipitation patterns. The downside of large-scale hydropower projects is potential habitat disruption, displacement of communities and altered river ecosystems (Smith, 2024). Geothermal energy for power production stems from the heat arising from the earth's interior. It is limited by geographic location availability of geothermal potential and suitability of geological conditions. On equal measure, the high upfront drilling costs, resource variability, and the potential for depleting reservoirs are challenges (Kabeyi, 2019).

Wind energy is abundant and emits no greenhouse gases during operation. However, wind power's intermittency and variability require energy storage solutions or backup power sources. The visual and noise impacts of wind turbines, along with the potential of having bird and bat collisions, can lead to potential opposition by the local residents and interested

organizations (Sander *et al*., 2024). Finally, wind is highly dependent on the weather conditions. Among these, solar energy has been preferred due to its abundance and low operation costs once installed. As a result, solar photovoltaic (PV) panels have become increasingly affordable making solar energy a competitive choice in the current market. Additionally, if all incident photons from the sun can be converted to electricity, an hour of consistent illumination would certainly meet the annual global demands for power (Roy *et al*., 2020). This makes the usage of PVs a promising power generation strategy since they efficiently convert sunlight directly into electricity.

Solar radiation as opposed to wind or hydropower is not location dependent and is available almost anywhere on earth. It is also ecosystem friendly and does not disrupt water habitats unlike hydropower. Additionally, the efficient conversion of sunlight to electricity using solar panels makes them a suitable choice as opposed to wind and hydropower which depend on kinetic energy conversion to electric energy, an energy transfer process which is prone to losses. However, the production of solar energy is limited to daytime hours which require batteries for storage. Solar energy is still evolving, and research is underway to improve their power conversion efficiency (PCE), stability in ambient conditions and cost reduction. The categories of solar cells according to their development stages include the first, second and third generation cells. In 1954, crystalline silicon (c-Si) based solar cell was developed in Bell lab, USA as the first-generation solar cell (SC) and had a PCE of 4.5% (Chapin *et al*., 1954). They exist in two forms as either single crystal or multiple crystal.

Thin films are reported to be the second generation SCs and include gallium arsenide (GaAs), cadmium telluride (CdTe), copper indium gallium selenide (CIGS) and amorphous silicon (a-Si). The thin film technology which is a second-generation solar cell technology is cheaper but is not as efficient as the conventional c-Si technology owing to its lower PCE in comparison. However, high cost, complicated technology and the non-eco-friendliest nature of the first two solar cell generations limit their usage (Kumar *et al*., 2021). Due to these factors, scientists have been trying to come up with solar cells with improved efficiency that are also cost friendly hence the emergence of third generation solar cells.

The third-generation solar cells emerged as a promising alternative with dye-sensitized solar cells (DSSCs) toping that list for some time. Other solar cells in this category are the organic solar cells (OSCs) and PSCs. DSSCs ability of being fabricated using simple processing conditions makes it a competitive choice compared to its counterparts. The process also accommodates low cost materials with structural tunability (Al-Ghamdi *et al*., 2021). The downside of this technology is the presence of liquid electrolytes which potentially leads to

instability. In addition to this, they exhibit low PCE which discourages their further development. The OSCs on the other hand features solution-processable, cost-effective, large-scale devices which are compatible with flexible substrates. Unfortunately, these OSCs could not achieve high PCE and have a shorter lifetime. PSCs have exhibited a number of advantages including higher efficiencies, low-cost raw materials, and don't involve complicated processing conditions (Zhou *et al.,* 2018). Owing to this and in recent times, they have been considered the most competitive third-generation solar cells. The performance and the power being generated by PSCs has gotten past the efficiency of the popular DSSCs, which is 12.3% (Tomar *et al*., 2020) in line with that of leading silicon solar cells which now stand at 26.1% (Cao *et al*., 2023). Spin coating, screen printing and other cheaper fabrication methods such as dip coating, thermal evaporation and many more can be applied in PSC fabrication (Roy *et al*., 2020). These processes can be performed in regular laboratories and do not require complicated technology.

Perovskites are compounds that have ABX_3 as their general formula. Here, A, B and X are three different species where A and B are positively charged ions and and X is a negatively charged ion. In 1839, calcium titanate ($CaTiO_3$) mineral was discovered by Gustav Rose, a German who specialized in the science of minerals. The chemical formula of PSCs closely resembles that of this mineral (Olaleru *et al*., 2020). PSCs offer prodigious promises for achieving high PCEs and transforming the solar energy landscape by topping the list of advancements in photovoltaic technologies. PSCs are a captivating discovery owing to their PCE which has risen gradually from 3.8% to 25.2% in the last decade (Roy *et al*., 2020), as opposed to other technologies which took a longer time to record the same. Despite all the merits, they still suffer from poor device stability, short lifetime, and toxicity of lead which have become hindrances to their commercialization. Lead free PSCs are a suitable alternative as they are cost effective, have high efficiencies and are non-toxic in nature (Gupta *et al*., 2021).

So far, lead based perovskites are popular due to their exceptional optical and electronic properties achieving conversion efficiencies of more than 20% (Nishimura *et al*., 2020). The toxicity associated with lead metal of these PSCs as well as their lifecycle is a serious concern, thus, research is being conducted to come up with stable, cost effective and ecofriendly PSCs. A number of low-toxicity cations have been suggested in place of lead metal in perovskites and Sn metal-based perovskites have shown the highest efficiency (PCE > 14%) and are gravitating towards 20% PCE (Jiang *et al*., 2021). Cesium-based all-inorganic PSCs are most preferred due to their superior thermal and phase stability (Zeng *et al*., 2019). The perovskite layer formed when a solution containing the perovskite sample is placed onto ETL or HTL and then

permitted to crystallize plays a key role in the conversion process. This perovskite layer serves as the main material for light absorption in the device as it absorbs light generating electron-hole pairs. Several key components and layers are involved in the fabrication of a PSC, where each layer serves a specific purpose in the energy conversion process.

In this study, cesium tin triiodide ($CsSnI_3$) perovskite is doped with germanium to exert control over tin (Sn) oxidation and charge carrier recombination which are suspected to degrade the stability of the PSC according to Seyed-Talebi *et al*., 2021. Their study further suggested that all inorganic perovskite materials can minimize device resistance, charge recombination and are cost effective. Therefore, the all-inorganic PSC synthesis in this study was done via a low-cost solution mixing process followed by thermal evaporation for electron transport layer (ETL) deposition. The absorber layer was deposited using the spin coating technique and the same was applied for the hole transport layer (HTL) deposition. Screen-printing technique was applied for graphite back electrode deposition. Between the HTL and ETL lied the perovskite layer. Owing to their affordability and good band alignment with the perovskite layer, fluorine-doped tin oxide (FTO) was used as a front contact, graphite as back metal contact and cuprous oxide (Cu_2O) as the hole transport material (HTM) (Sabbah, 2022).

1.2 Statement of the Problem

Lead metal (Pb) is classified as one of many poisonous metals and has been flagged among the ten dangerous, life threatening chemicals by Restriction of Hazardous Substances (ROHS). In addition to this, the European Union's obligations discourage involvement of dangerous materials in the fabrication of electronic and electrical devices. Pb-based perovskites if badly disposed, can produce soluble Pb containing chemicals easily into water (Wu *et al*., 2022). This makes them bioavailable and could lead to serious ecological pollution since they are easily absorbed by plants and affect the food cycle circulation. Among the alternatives to lead, Sn based perovskites are viable due to their favourable optoelectronic properties. Nevertheless, $CsSnI_3$ inherent instability and limited performance have hindered its practical application in solar cells. This study proposed tackling this significant challenge of instability in $CsSnI_3$ perovskite solar cells by incorporating germanium (Ge) as a dopant into the $CsSnI_3$ absorber layer. The selection of Ge as a dopant was based on its potential to curb Sn oxidation hence enhancing the stability and performance of Pb-free perovskites.

1.3 Objectives

1.3.1 General Objective

To fabricate and evaluate a perovskite solar cell that uses a Ge-doped $CsSnI_3$ perovskite layer for efficiency and stability enhancement.

1.3.2 Specific Objectives

i. To deposit tin (IV) oxide ETL on the FTO glass substrates and determine the optical properties.
ii. To deposit germanium doped cesium tin triiodide absorber layers on FTO glass substrates and determine the optical properties.
iii. To evaluate the structural and morphological properties of the deposited germanium doped cesium tin triiodide absorber layers.
iv. To fabricate a perovskite solar cell and evaluate its photovoltaic parameters.

1.4 Research Questions

i. What are the optical properties of tin (IV) oxide ETL and how does the thickness affect the transmission of incident light?
ii. What are the optical properties of germanium doped cesium tin triiodide absorber layers.
iii. What are the structural and morphological properties of the germanium doped cesium tin triiodide thin films and how does the variation of spin coating speed influence these properties?
iv. What are the photovoltaic parameters of the fabricated PSC using the optimized ETL and perovskite layer?

1.5 Justification

The instability of $CsSnI_3$ has hindered its practical application in solar cells. $CsSnI_3$ undergoes oxidation and phase transition especially at high temperatures leading to increased recombination process and formation of less stable phases (Nishimura *et al*.,2020). By replacing Pb and doping $CsSnI_3$ with Ge, this study aimed to minimize Pb's toxicity to the environment and potentially enhance the stability of the perovskite by reducing charge recombination losses. This could lead to improved device performance. The findings in this study have contributed to the growing field in renewable energy technologies and encourages research in upcoming PSCs innovations. Many nations are aiming a sustainable and resilient energy future and this research aligns with this by reducing toxicity, promoting cost effectiveness and potentially enhancing stability in PSC technology. This goes hand in hand with Sustainable Development Goal (SDG) 7 that advocates for access to clean and affordable energy.

CHAPTER TWO
LITERATURE REVIEW

2.1 Structure of the PSCs

The two principal device structures that have signified promising performance as a result of extensive investigations are the inverted structure (p-i-n) and the planar heterojunction (n-i-p). The perovskite films are prepared through deposition methods such as vapor deposition (Guo *et al*., 2017), spray coating (Suazo *et al*., 2020), spin coating (Zhang *et al*., 2016), blade coating (Li *et al*., 2018), inkjet printing (Gribkova *et al*., 2019) among others. For the n-i-p structure between the HTL and ETL, lies the perovskite layer as shown in Figure 2.1 (a) (Nair *et al*., 2020). A conductive electrode is then deposited on the ETL. Song *et al*. (2017) reported an n-i-p structured PSC with $CsSnI_3$ perovskite layer synthesized in hydrazine atmosphere. Here, the perovskite film was sandwiched between titanium (IV) oxide (TiO_2) ETL and poly[bis(4-phenyl) (2,4,6-trimethylphenyl) amine] (PTAA) HTL. There after a PCE of 3.89% was achieved for the PSCs with gold electrodes deposited via thermal evaporation method on the ETL.

The case for inverted PSCs is not the same as the HTL is normally coated on TCO. The perovskite film is then deposited on the HTL followed by the deposition of the ETL. This device structure circuit is then finalized by a metal contact or carbon as seen in Figure 2.1 (b) (Chowdhury *et al*., 2022). Low hysteresis has been observed in PSCs with the p-i-n structure (Dixit *et al*., 2022). Due to higher charge carrier mobility and shorter diffusion length of the perovskite film, this PSC exhibited high light soaking stability and PCE. Yin *et al*., (2021) investigated a Sn based inverted PSC with $CsSnI_3$ perovskite layer and achieved a high PCE of 8.2%. This PSC of the structure ITO/PEDOT: PSS/Perovskite/C60/BCP/Cu was also highly stable.

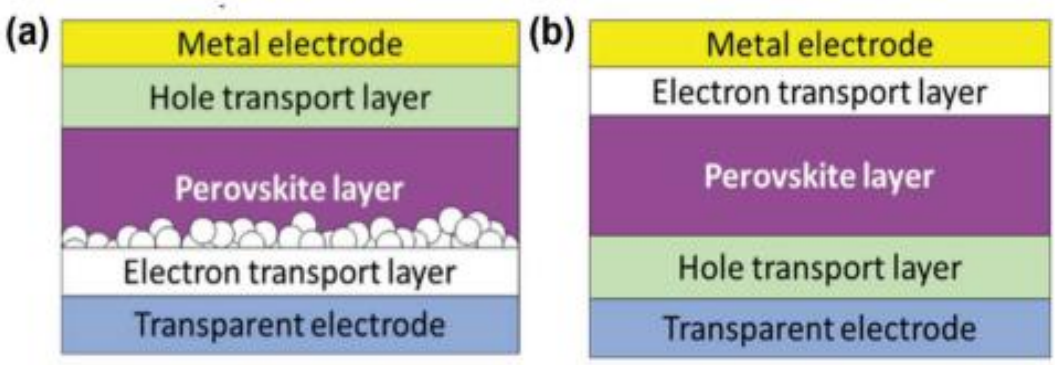

Figure 2.1: PSCs architecture (a) n-i-p (b) p-i-n
Source: Chowdhury *et al*. (2022)

The choice of HTL material is essential especially in the stability of p-i-n structured PSCs (Marshall *et al*., 2017). They assembled an inverted structured PSC with $CsSnI_3$ as the perovskite film and copper (I) iodide (CuI) as the HTL. They found that the CuI prepared via solution process was not a good match in $CsSnI_3$ PSCs. The results revealed that this was due to the $CsSnI_3$ precursor solution dissolving the CuI and destroying it during the spin coating process. The ETL also plays an equally important role in the p-i-n structure. Marshall *et al*. (2015) reported an inverted structured PSC with fullerin ETLs and concluded that the ETLs are important in controlling the V_{oc} of the PSC. This was because of the energetics at the interface between the ETL and the perovskite films. Seyed-Talebi *et al*. (2021) investigated the performance of a PSC with different HTLs with cesium tin germanium triiodide ($CsSnGeI_3$) as the perovskite layer. He found that the charge extraction at the interfaces of the layers was affected by energy level mismatches between the charge transport and perovskite layers.

Therefore, the choice of solar cell structure directly affects the stability of PSCs and how efficiently they convert sunlight into electricity. Performance, efficiency, and stability of both inverted and conventional PSCs highly depend on the type of perovskite thin film, preparation technique of perovskite layer, the ETL and HTL materials.

2.2 Deposition of Perovskite Thin Films

Achieving high-quality perovskite films is crucial for optimizing PSC performance since it significantly influences the superior physical and optoelectrical properties of the solar cells. The characteristics of perovskite thin films encompass morphology, crystallinity, and composition. Hence, researchers have dedicated their efforts to control the crystallinity and morphology of these films (Eperon *et al*., 2014; Sharenko & Toney, 2016). The morphology and crystallinity rely on variables like deposition techniques, deposition conditions, chemical composition, annealing temperature, growth mechanism among others (Cao *et al*., 2019; Dubey *et al*., 2018). Perovskite thin films are typically deposited using two primary approaches: vapor deposition and solution-based methods.

Solution-based coating techniques such as spin-coating, spray coating, blade-coating or slot-die coating have been reported as possible technics used for deposition of perovskite films (Jiang *et al*., 2022). Spin coating is commonly used because it is easy to operate and is cost effective (Zhang *et al*., 2016). These coating methods are classified as either one-step or two-step. The key control factors In the one-step method include the annealing temperature, the solvent type, molar composition, and the timing and quantity of anti-solvent dripping (Krishnan *et al*., 2019). To expedite the crystallization process, anti-solvents like toluene, ethyl acetate

and chlorobenzene have been used (Howlader *et al*., 2022). Song *et al*. (2017) used the one step spin coating method in a weak hydrazine atmosphere to deposit $CsSnI_3$ films with varying cesium (II) iodide/ tin (II) iodide (CsI/SnI_2) ratios mixed in dimethylformamide (DMF) and dimethylsulfoxide (DMSO) solvents. The ratio of CsI varied from 0.2 M to 1 M and the amount of SnI_2 was at a fixed value of 1 M. A wide range of ratios resulted in the formation of good coverage films.

Lee *et al*. (2017) investigated a two-step deposition of cesium tin (IV) iodide (Cs_6SnI_6). This involved the deposition of CsI first followed by the deposition of SnI_4 in the second step process. Spin coating, electro spraying and drop casting were first employed to deposit CsI films. From the morphological results, notable clusters of CsI were seen in the spin coated film with the electro sprayed films exhibiting pure CsI crystals. The drop casting method resulted in branched crystalline structures of CsI. The deposition of SnI_4 in the second step involved the immersion of SnI_4 solution in the CsI deposited layer. Spray coating has also been reported to deposit CsI and SnI_2 reactant combination in DMF solvent which resulted in the formation of a pure phase Cs_6SnI_6 thin film (Suazo *et al*., 2020). This was caused by the low temperature deposition and an excess of SnI_2 facilitated by the spin coating method. Despite the reported advantages of spin coating, poor morphology resulting from one step spin coating method has been reported (Jung *et al*., 2019; Liang *et al*., 2017).

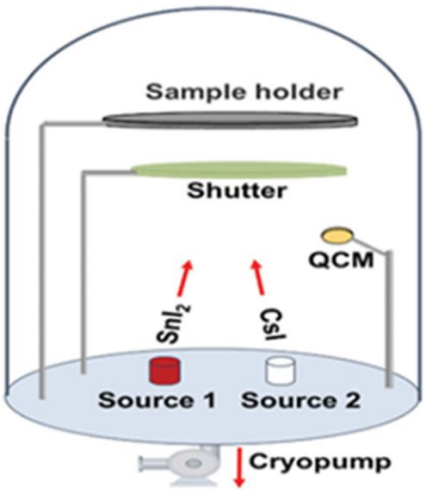

Figure 2.2: Two step dry process for Cs_6SnI_6 film deposition

Source: Guo *et al*. (2017)

Vapor deposition technique involves the fabrication of the perovskite in a furnace/chamber without the utilization of any solvent with vacuum conditions. It is quite analogous to the two-step technique the only difference being that in vapor deposition method, precursors are deposited using a vapor deposition approach and is not a solution process unlike

the two-step technique. This method has resulted in perovskite films with a uniform and smooth morphology (Liu *et al*., 2013). $CsSn_{0.5}Ge_{0.5}I_3$ powders deposited via thermal evaporation resulted in uniform coverage films which were highly stable (Chen *et al*., 2019). Thermal evaporation is preferred in the deposition of Sn based perovskites due to their sensitivity to air. Co-evaporation deposition technique can achieve a pure phase from a combination of CsI and tin (IV) iodide (SnI_4) precursors, but SnI_4 can thermally decompose on heating (Lopez-Fraguas *et al*., 2019). This could result in a non-uniform surface coverage of the perovskite layer. They concluded that the deposition method used in $CsSnI_3$ synthesis affects its stability arising from the issue of oxidation of $CsSnI_3$ to Cs_6SnI_6. Guo *et al*. (2017) investigated the formation of Cs_6SnI_6 by co-depositions of CsI and SnI_2 powders inside a furnace as seen in Figure 2.2. The deposition was followed by annealing in I_2 vapor to achieve a pure film. The resultant thin films from this two-step dry process had a better morphology compared to films prepared with the gradual oxidation of orthorhombic $CsSnI_3$.

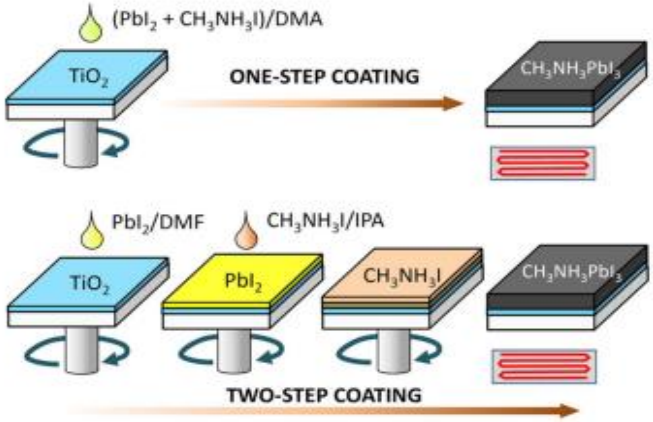

Figure 2.3: Spin coating of $CH_3NH_3PbI_3$

Source: Im *et al*. (2014)

Zhu *et al*. (2018) used both the solution method and vapour deposition technique to deposit $CsSnI_3$ films. They deposited SnI_2/tin (I) fluoride (SnF) solution first using the spin coating method then applied thermal evaporation of CsI. This resulted in a dense perovskite thin film with large crystal grains and good coverage. Figure 2.3 serves as a visual representation of both the one-step and two-step spin coating techniques. In the context of the two-step approach, a significant drawback arises from its limited ability to effectively regulate the uniformity and crystalline quality of thin films, leading to inconsistencies (Nair *et al*., 2020). In the realm of producing perovskite thin films, the one-step method is typically favoured due to the numerous benefits it provides. These advantages encompass consistent surface morphology, cost-effectiveness, precise control over crystallinity and composition.

2.3 Insights from Perovskite Research

Oxide perovskites are considered due to their multipurpose nature, but their photovoltaic performance is limited because their band gap is wide making them harvest only 2.8% of the solar radiation spectrum (Chen *et al*., 2015). For this reason, inorganic halides; chlorine (Cl), iodine (I) and bromine (Br) are preferred as X site anions due to their strong light absorption properties, higher charge carrier mobility and better optoelectronic properties thus the use of iodine in this research. In most cases methylammonium (MA) is generally at site A, formamidinium (FA), rubidium (Rb) or cesium (Cs) are also suitable while B site are mostly tin (Sn^{2+}) and lead (Pb^{2+}) cations. Cs is preferred as a substitution of the common organic cations as studies have shown that it enhances thermal stability and ambient outdoor performance of the solar device (Sabbah, 2022). It is known to be stable up to about 400^{o}C, but MA and FA degrade speedily at 200^{o}C (Chen *et al*., 2019).

Due to the toxicity of lead as a B site cation, several cations which are low in toxicity have been proposed. This includes silver (Ag), bismuth (Bi), antimony (Sb), titanium (Ti), germanium (Ge) and Tin (Sn) (Chen *et al*., 2021). Chen *et al*. (2021) reviewed tin-based perovskites in particular because apart from low toxicity, Sn based perovskites have great electrical and optical properties. They found that, in comparison to Pb, Sn has a similar type of electron valence configuration (ns^2sp^2) as well as close ionic radii 1.18 Å and 1.19 Å for coordinated six Sn^{2+} and Pb^{2+} ions respectively. Goldschmidt tolerance factor (t) was used to determine the structural stability of $CsSnI_3$ and $CsPbI_3$ perovskites (Wang *et al*., 2022) using the equation:

$$t = \frac{r_A + r_X}{\sqrt{2}(r_B + r_x)} \tag{2.1}$$

Where r_A, r_B and r_x represent the ionic radii of the A, B and X perovskite species respectively. The closer the t value to unity, the more stable it is. After investigation, $CsSnI_3$ perovskite displayed a value closer to 1 as with reference to the $CsPbI_3$ perovskite. This was attributed to the ionic radius of Sn^{2+} being smaller than that of Pb^{2+}. Therefore, $CsSnI_3$ perovskite showed better stability. Zuo *et al*. (2014) investigated a mixed Pb-Sn n-i-p structured PSC. They did this in consideration that both Sn and Pb have similar qualities coming from the same group of the periodic table. They observed that Sn has higher mobilities of 100-1000 cm^2 /Vs when utilized in perovskites as compared to lead which has mobilities of 10-100 cm^2 /Vs. Therefore, Sn metal was preferred in this research.

However, despite these positive characteristics of Sn based perovskites, the rapid oxidation of the vacancies of Sn^{2+} ions in the presence of oxygen is a challenge. Sn^{2+} oxidizes

to Sn^{4+} in the presence of oxygen, the oxidized Sn^{4+} behaving as a p-type dopant which leads to increased recombination (Leijtens *et al*., 2017). As a result, Shao *et al*., 2018 investigated this and succeeded in the reduction of the background hole density by more than one order of magnitude. They achieved this by synthesizing a mixed 2D/3D tin based $FASnI_3$ PSC. This improved the stability of the PSC and a PCE of 9% was achieved. The performance of Sn based for FA PSCs was investigated by adding ethyl ammonium (EA) cations into the 2D/3D mixed perovskite films. This led to enhanced crystallinity and orientation of the perovskite films. This device also exhibited less hysteresis and light soaking. Ge was used as a dopant in a Sn based perovskite with mixed cations (Nishimura *et al*., 2020). This led to the suppression of defects and traps with the best device, achieving a PCE of 11.75% and a V_{oc} of 0.7 V.

Chiara *et al*. (2021) reviewed Ge based halide perovskites and found that with respect to Pb, abundant Ge has little toxicity and environmental concerns. $CsSn_{0.5}Ge_{0.5}I_3$ was used in fabrication of a Pb-free PSC and it was found that the addition of Ge plays a key role in the improvement of the efficiency of solar cells. It enhances the surface morphology and in turn the quality of the films (Chen *et al*., 2019). The group achieved a PCE of 7.11% and the PSCs demonstrated high stability after 500 h of continuous operation in a nitrogen atmosphere showing a less than 10% efficiency decay. Nishimura *et al*. (2019) investigated Ge doped $CsSnI_3$ PSC and found that addition of 5mol% Ge induced a long-lived carrier lifetime (τ=5.04 ns), longer carrier diffusion length exceeding 1 µm and higher mobility of 98.27 cm^2 /Vs as compared to the undoped perovskite. The trap density was also reduced from 10^{15}-10^{17} cm^{-3} to 10^{8}-10^{14} cm^{-3} with Ge doping. Ge^{2+} ions suppress Sn^{2+} vacancies of the $CsSnI_3$ perovskite layer by filling them resulting in passivated trap states which lessens V_{oc} loss for higher PV performance.

The resultant $CsSnGeI_3$ perovskite composition according to perovskite experiments, has shown great stability in continuous operation under 1-sun illumination for 500 h plus (Seyed-Talebi *et al*., 2021). Exposing this resultant perovskite layer to air causes a native oxide layer to form on the surface in 30 s which leads to an increase in PCE of the solar cell up to 7.11% (Seyed-Talebi *et al*., 2021). According to Chen *et al*. (2019), the native oxide layer serves as an interfacial layer between the HTL and absorber layer having a wide band gap with a resultant fill factor of 0.606 and open circuit voltage (V_{oc}) of 0.63 V.

Chen *et al*. (2019) suggested a $CsSnGeI_3$ perovskite material that demonstrates better performance and remarkable resistance to degradation in the presence of air compared to $CsSnI_3$ and $CsGeI_3$ pure counterparts with a PCE of 7%. He also found the band gap to be 1.50 eV which is suitable for visible light absorption (Chen *et al*., 2019). However, an increase in

Ge doping beyond 5% leads to decrease in electronic properties i.e. poor charge transport (Nishiamura *et al*., 2019). The thicker Ge on the perovskite layer surface led to high resistance in performance hindering the charge transport process. Tin SnO_2 has been used as an electron transport material (ETM) in this research as it keeps better band alignment with the $CsSnGeI_3$ perovskite layer and has a high electron mobility. According to Wang *et al*. (2021) this supports electron extraction and additionally has applicable conduction and valence bands, is of low cost and their production process is simple and easy.

Zuo *et al*. (2015) prepared Cu_2O and copper (II) oxide (CuO) via solution process to act as hole transport materials (HTMs) in PSCs. They also prepared poly(3,4-ethylenedioxythiophene): poly(styrenesulfonate) (PEDOT: PSS) HTL on $MAPbI_3$ perovskite layer then they evaluated and compared their performance. They determined that Cu_2O is a suitable HTM due to its natural *p*type conductivity and in comparison, to PEDOT: PSS, Cu_2O and CuO display higher V_{oc}, J_{sc} and PCE. They achieved PCEs of 12.16% and 13.35% when they used CuO and Cu_2O as HTMs respectively. Additionally, these PSCs showed improved stability. Higher crystallinity was observed for the perovskite films synthesized on top of the Cu_2O and CuO films resulting in enhanced charge carrier transport.

Uddin *et al*. (2024) reported a PSC with a PCE of 25.15% utilizing Cu_2O as HTL. The direct band gap structure of Cu_2O and its compatibility with several semiconductors (Hossain *et al*., 2023) could contribute to a high PCE. For these reasons, Cu_2O has been used in this study as a suitable HTM. The front electrode is normally a common conductive glass, majorly FTO or indium tin oxide (ITO) and both are known for their good electrical conductivity. Chen *et al.* (2022) reviewed the rare electrode materials used in PSC fabrication and noted that ITO is expensive. Therefore, FTO is preferred in this research as it is more cost-effective compared to ITO and this could be because of the use of simpler deposition processes and cheaper tin precursors with FTO.

Ku *et al*. (2013) investigated a PSC based on carbon back electrode. They preferred carbon electrodes due to their low cost, requirement of low temperature processing (100^oC), and high conductivity. Their work function (5.0 eV) is also close to that of which is 5.1 eV. They used screen printing method for carbon electrode preparation and the highly stable solar cells achieved PCEs of above 6.64%. The back electrode is commonly made of expensive gold (Au) or silver (Ag) metals. Best PSC performances have been reported using Au as the back electrode with efficiencies of up to 30.98% reported by Sabbah. (2022). He investigated the performance of a simulated PSC with Au as the back electrode. A review on the carbon-based materials for the synthesis of back electrodes noted that the expensive nature of Au and Ag

required scientists to look for alternative back electrodes to replace them (Bella & Fagiolari, 2019). Additionally, it was said that Ag and Au as back electrodes may negatively affect the performance of the solar cell due to the reaction with halides originating from the absorber layer. The carbon-based materials that are common in PSC applications are graphite, graphene, carbon nano tubes (CNTs) and amorphous carbon as reviewed by Bella and Fagiolari. (2019).

Some of the reported techniques to investigate the efficiency, optoelectronic properties and stability of PSCs are XRD, UV-Vis, atomic force microscopy (AFM), transmission electron microscopy (TEM), scanning electron microscopy (SEM) and J-V measurements (Boro *et al.*, 2022). XRD is used to investigate the crystal structure and to analyse the chemical composition of PSC layers. Joshi *et al.* (2021) studied the structural and crystallinity degradation of $CH_3NH_3PbI_3$ perovskite using XRD measurements with respect to time intervals of 5 days. The several peaks observed indicated the degrading of the perovskite layer on air exposure. Defect formation on the surface of the perovskite film can also be determined by XRD. The technique revealed grain size reduction of the perovskite layer when graphene contacted fabricated solar cell is exposed to light at air exposure for 30 and 45 days (Ghadiri & Gorji, 2020). According to the results obtained, the defect layer became thicker under the exposure.

UV-Vis spectroscopy is important as it measures the optical properties, that is, absorbance and transmittance of semiconducting materials (Boro *et al.,* 2022). $MAPbI_3$ absorbance behavior was investigated by Yang *et al*. (2015) using this technique under controlled relative humidity of 98± 2%. Reduction in absorbance was recorded at a wavelength of 760 nm and immediate bleaching at 500 nm. There was increased background absorbance above 800 nm and this showed the decomposition of $MAPbI_3$ due to formation of a large crystallite. SEM is used to study surface morphological properties and Howlader *et al*. (2022) investigated the morphology of $CsSnI_3$ thin films and found that a unique type of morphology is formed. Additionally, they found that the type of antisolvent treatment used influences the crystalline structure and surface uniformity of the perovskite thin film chlorobenzene showing the best results.

2.4 Stability of PSCs

The terms stability and degradation together characterize the conditions and issues influencing PSC availability, existence and commercialization. When it comes to stability, the PSCs drastically deteriorate after a few hundred hours of use (Domanski *et al*., 2018). After 500 hours of operation, they noted that the photovoltaic solar cells can only maintain 80% of their initial efficiency, even with the right coatings applied. Degradation intensifies over time,

resulting in a reduction in these solar cells' total performance and efficiency. The stability assessment uses the damp heat test, which requires 85°C temperature and 85% relative humidity, in accordance with the guidelines established by the International Electrotechnical Commission (IEC) (Mazumdar *et al*., 2021). According to these criteria, stable devices should exhibit no more than a 10% reduction in their power conversion efficiency (PCE) after being exposed for 1000 hours. However, hybrid PSCs are currently facing challenges in achieving this goal. The subsequent section explores the various factors that contribute to the instability of photovoltaic solar cells.

2.5 Aspects Distressing the Stability of PSCs

2.5.1 Effect of Moisture and Oxygen

The interface of the perovskite film incorporating water molecules and oxygen is one of the issues which arise in PSCs. It is an inevitable phenomenon which can occur during assembling and testing. Sn based perovskites have been reported to be prone to degradation on air exposure since the Sn^{2+} in methylammonium tin triiodide ($MASnI_3$) perovskite oxidizes to Sn^{4+} leading to high charge carrier recombination as documented by Leijtens *et al*. (2017). Their report analysed the oxidation process of $ASnI_3$ where A can be made of cations like Cs, MA and FA. On air exposure, the $ASnI_3$ disintegrates to SnI_4 gas and vacancies of Sn^{2+} and I^-. The chemical reaction that takes place with perovskite is as follows:

$$2ASnI_3 + O_2 \rightarrow 2AI + SnO_2 + SnI_4 \quad (2.2)$$

Leijtens *et al*. (2017) also investigated the degradation of formamidinium tin triiodide ($FASnI_3$) on heating at 70°C for 12 h in dry air. They demonstrated that Sn based perovskite materials undergo fast oxidation at high temperatures. The main degradation product of $FASnI_3$ was established to be SnI_4 observed from its unique absorption spectra. They concluded that the utilization of a smaller cation like Cs is said to slow down the oxidation of Sn^{2+} hence its preference in this research.

2.5.2 Temperature Effects

According to international standards, PSCs are required to exhibit long-term stability at 85°C to compete with the solar cells which are currently in the market (Wang *et al*., 2019). Therefore, temperature plays a crucial role in determining the overall efficiency of photovoltaic solar cells. Annealing is a fundamental step when creating perovskite films, making perovskite materials susceptible to high temperatures exposure. The structural stability of $CsSnI_3$ can be altered as a result of temperature change as reported by Chowdhury *et al*. (2022). When subjected to a temperature of about 500 K, this perovskite converts to a black cubic phase. As the temperature decreases to 380 K a black tetragonal phase is formed and a black/yellow

orthorhombic phase forms on further temperature decrease to 300 K. Figure 2.4 (Chung *et al*., 2012) is an illustration of the phase transition of the four polymorphs of $CsSnI_3$. Cs atoms are represented in blue, Sn atoms in yellow and I atoms in violet. The green dashed lines represent a unit cell.

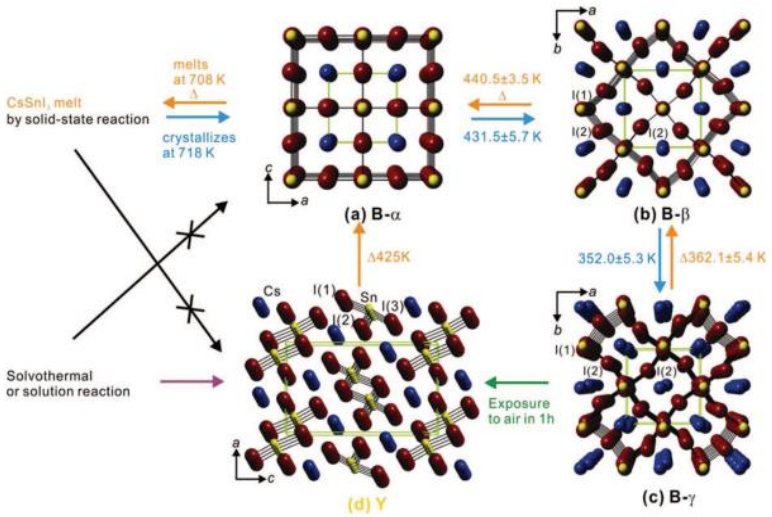

Figure 2.4: Crystal structures of the $CsSnI_3$ (a) black cubic phase (500 K); (b) black tetragonal phase (380 K); (c) black orthorhombic phase (300 K); (d) Yellow orthorhombic phase (300 K) Source: Chung *et al*. (2012)

Chung *et al*. (2012) found that the black orthorhombic phase is the most stable phase at room temperature. They investigated the phase transitions of $CsSnI_3$ using temperature dependent XRD and differential thermal analysis (DTA). The phase transition between the black phases is reported to be reversible in an inert atmosphere and relies on temperature. The pure black and yellow orthorhombic phases are reported to only occur as a result of solution reactions and solid-state reactions respectively. They further suggested that the possible phase transition between the black orthorhombic phase to the yellow orthorhombic phase occurs on air or moisture exposure at room temperature. This can also occur during synthesis on reaction with organic solvents at room temperature. In a reverse investigation, to achieve the black phases from the yellow phase, heating was done to about 500 K.

2.5.3 Toxicity

Lead toxicity has a negative effect on our environment and can cause serious health risks. Upon exposure of Pb to rainwater, it dissolves in the water leaving behind insoluble PbI_2. This contaminates the soil and groundwater affecting plants and other living organisms (Yue *et al.,* 2023). Generally, this PSC will comprise around one third lead by weight. A panel of PSCs releases only 70 ppm of lead and as compared to the standards, this concentration is

moderately low. Despite it not being disastrous, there is no agreed safe threshold for lead exposure. Caution needs to be exercised to avoid exposure, and this is linked to the commercialization of the PSCs (Babayigit *et al.*, 2016). The exposure of lead is associated with symptoms such as nausea, abdominal pain, neurological deficiencies, vomiting, headaches, reproductive defects, seizures, genotoxicity, muscle weakness and carcinogenicity (WHO, 2010). Zhang *et al*. (2024) reported that the degraded products resulting from the Pb based perovskites ($CsSnI_3$, $MAPbI_3$, and $FAPbI_3$) are highly toxic to the ecosystem, a big challenge in their commercialization.

The solvents employed in the production of photovoltaic solar cells can be categorized as either precursor solvents or antisolvents and are essential in the synthesis of perovskites. However, a significant challenge arises from the toxic nature of most solvents in this category, posing a hindrance to the widespread application of this technology. Among the commonly used solvents are DMF, DMSO and γ-butyrolactone (GBL). Unfortunately, these solvents are harmful to both human health and the environment (de Ménorval *et al.,* 2012). This creates a concern as they elevate the bioavailability of Pb, putting frontline workers at an increased risk of exposure through dermal contact and oral ingestion.

DMF is one of the most harmful among all the listed solvents employed in the fabrication procedures of PSCs (Jones *et al.,* 2016). However, a mixture of DMF and DMSO is known to enhance the morphology of perovskite films in perovskite precursor solutions. DMSO coordinates with Pb^{2+} whereas DMF is used in the improvement of dissolution of PbI_2 therefore, despite its well-known toxicity, the application of DMF is necessary in the fabrication process (Cao *et al.,* 2022). Inhalation or skin contact to DMF can cause harmful health problems such as vomiting, palpitations, anxiety, skin irritation, nausea, flushing headache, and liver problems (Lauwerys *et al.,* 1980). Generally, volatile organic solvents mostly used in high efficiency PSCs are highly toxic hence it is important to explore available alternative solvents or other methods that can reduce the use of these solvents in the PSC fabrication process.

2.5.4 Device Encapsulation

Encapsulation refers to the process of protecting the active perovskite layer and other sensitive modules of the solar cell from exposure to external environment. It serves an important role in improving the long-term stability and durability of PSCs by preventing degradation due to moisture, oxygen, light, and other environmental factors (Chen *et al*., 2017). Moisture intrusion into the PSC is the most important purpose of encapsulation since moisture serves a destructive role in the degradation and stability of the device. Lee *et al*. (2018)

investigated the performance and stability of PSCs with encapsulation and without encapsulation. Testing was conducted at 50°C with a RH exposure of 50% for a period of 300 h. Their results revealed that the PSC without encapsulation displayed a FF of 38.6% down from 79.6 %. It only retained 48% of its efficiency after the period. They also suggested some of the factors that could contribute to a successful encapsulation which include no thermal damage to the solar cells, possession of high-water transmission rate and be high transparency to allow maximum light penetration.

Encapsulation deems necessary because even the PSCs fabricated based on the most stable compositions still degrade on exposure to ambient air (Cheng *et al.*, 2019). While moisture-resistant layers can provide some level of effectiveness in guarding against moisture infiltration within the cell, they fall short in completely preventing the ingress of oxygen. This underscores the vital importance of sealing photovoltaic solar cells.

2.5.5 Charge Recombination

Charge recombination denotes a process where electron and hole charges generated recombine and lose energy as light or heat instead of being efficiently extracted and utilized to generate electricity. The electron-hole recombination process is characterized by the loss of useful carriers. The phenomenon can be easily grasped through the following explanation: when an electron is energized by absorbing radiation and moves to the conduction band, it enters a temporary state of higher energy known as a metastable state. This electron then attempts to attain a more stable position with lower energy within the valence band. The excited electrons transition from the conduction band to the valence band, where they occupy previously unoccupied states, resulting in a reduction of current and overall efficiency in the cell. The recombination process, which involves the combination of electron-hole pairs, is influenced by a range of factors. These factors include the energy levels of materials responsible for extracting charges, defects existing in both the bulk material and at interfaces, charge mobility within the perovskite and/or contact materials, as well as the distance over which charges diffuse before recombining. (Aftab & Ahmad, 2021)

Sn^{2+} oxidation is the most common cause of defects linked to Sn based perovskites and can be evaluated using hall effect measurements (Chung *et al.*, 2012). Kumar *et al.* (2014) fabricated a PSC with $CsSnI_3$ perovskite doped with different concentrations of SnF_2. This resulted in a PCE of 2.02% and a J_{sc} of 22 $mA.cm^{-2}$ and this performance was attributed to severe charge recombination which led to the degradation of the cell. The high density of defects possibly resulted from the native oxidation of Sn^{2+} to Sn^{4+}. They found that the background hole density was minimized with increasing SnF_2 content resulting in increased

carrier density and mobility. The categorization of recombination is based on different mechanisms and the nature of the recombination process. There are three primary classifications of recombination: radiative, non-radiative (also known as Shockley-Read-Hall), and auger recombination. Radiative recombination occurs when an electron in the conduction band directly recombines with a hole in the valence band, leading to the emission of photons with energy equal to the bandgap. In contrast, non-radiative recombination (Shockley-Read-Hall recombination) takes place through an alternative path involving defects in the material like grain boundaries, impurities and dislocations (Tress *et al*., 2015).

Auger recombination involves the combination of an electron and a hole, releasing energy that propels the ejection of a third carrier. This third carrier typically loses energy and settles at the conduction band edge. Another perspective on recombination includes monomolecular and bimolecular charge carrier recombination at the molecular level. Monomolecular recombination involves an individual "particle" like a conduction-band electron or an already formed exciton—a bound electron-hole pair. On the other hand, bimolecular recombination predominantly involves interactions between electrons and holes within a direct bandgap semiconductor. This process can occur on its own without influence and results in the emission of photons. It is intricately connected to the reverse mechanism of light absorption (Aftab & Ahmad, 2021).

Charge carrier recombination equation of dynamics can be expressed as:

$$\frac{dn}{dt} = G - k_1 n - k_2 n^2 - k_3 n^3 = G - nR_T(n) \tag{2.3}$$

Here, G signifies the rate of charge density generation, k_1 is denoted as the rate of monomolecular charge recombination, k_2 represents the constant for bimolecular electron-hole recombination, and k_3 signifies the rate constant for Auger recombination whereas $R_T(n)$ signifies total charge recombination rate. It can be written in the form of an equation as:

$$R_T = k_1 + k_2 n^2 + k_3 n^3 \tag{2.4}$$

Charge recombination rate is dependent on other factors such as charge carrier density (n), time t, product of free electrons and holes concentration. On the other hand, Auger non-radiative recombination is not common in PSCs and can be ignored. Shockley-Read-Hall (SRH) on the other hand happens frequently in PSCs (Aftab & Ahmad, 2021). Tress *et al*. (2015) demonstrated a V_{oc} loss of 200 mV in $CH_3NH_3PbI_3$ perovskite after recording a V_{oc} of 1.1 V approximately 0.2 points lower than the theoretical limit of 1.32 V which was attributed to non-radiative recombination as a result of non-selective contacts.

2.5.6 Hysteresis

It refers to the current voltage difference characteristics of a PSC when sweeping voltage in a forward direction (from low to high) as compared to the reverse direction (from high to low). This hysteresis effect can manifest as a shift in the J-V curve and can have implications for device efficiency and long-term stability. Hysteresis shows that the measured efficiency depends on the direction. Hysteresis is determined by hysteresis index (HI) which is illustrated by the equation (Aftab & Ahmad, 2021):

$$\mathrm{HI} = \frac{\mathrm{PCE_{rev}}}{\mathrm{PCE_{for}}} - 1 \tag{2.5}$$

Where $\mathrm{PCE_{rev}}$ is PCE for reverse scan and $\mathrm{PCE_{for}}$ is PCE obtained in forward scan. The hysteresis observed in the J-V curve is believed to stem from several potential factors, primarily including the gradual migration of cations and anions as well as the entrapment of ferroelectric polarization charges. It is universally accepted that:

i. The eventuality of hysteresis in perovskite cells is heavily reliant on unique arrangement of the device. It is notable on charge-selective contact layers, within the perovskite bulk, and at various interfaces involving heterojunctions, such as perovskite/ETL or perovskite/HTL.
ii. Changes in the structure of the perovskite when functioning as part of a solar cell could be responsible for the hysteresis.
iii. The change detected in the current-voltage (I-V) curve during forward and reverse scans, commonly attributed to the solar cell's capacitance, can contribute to hysteresis.
iv. Scanning rate and direction affect the degree of hysteresis. Hysteresis usually decreases with decreasing scan rates.

In addition to the typical hysteresis pattern, an inverse hysteresis displaying opposing behaviour has also been seen; nevertheless, the precise source of hysteresis is still up for discussion. According to Krishnan *et al.* (2019) the formation of interfacial charge extraction barriers brought on by the accumulation of space charges and ionic defects are the causes of this inverse hysteresis. Different bias scan circumstances cause changes in ion mobility at the interface between the perovskite and the HTL or ETL. These circumstances influence how these hysteresis effects are modulated.

Dixit *et al*. (2022) reported that defects arising from PSC fabrication attract the hysteresis effect. They also reported that the phase change/ decomposition of the perovskite layer could be another reason contributing to the effect. The J-V scan settings can affect the

device functionality in that, a scan from open circuit to closed circuit can alter the V_{oc} and the vice versa is true for the same PSC (Xi *et al*., 2017). The p-i-n perovskite structure is more prone to hysteresis than the mesoporous structure. This was suggested by Jena *et al*. (2019) because on polarization of the p-i-n structure, a negative polling effect is observed as well as a forward and reverse scan hysteresis. This is due to the weaker ferroelectric properties in the mesoporous structure with a high random dipole arrangement. In a mesoporous structure, the slow charge transfer process that easily leads to hysteresis is eliminated by the separation of charges.

2.6 Commercialization of the PSCs

Commercialization is an important factor after the fabrication of PSCs and it is dependant on three pivotal factors: device performance, cost, and stability. Notably, strides in device structure, synthesis and fabrication processes have elevated device performance, thereby propelling perovskite solar cells toward an inexorable trend of commercialization. This growth has seen PSCs transition from laboratory settings to the realm of commercial markets. These solar cells exhibit enhanced device performance alongside remarkably economical production costs. While device stability has posed challenges for both researchers and industries, substantial progress has been achieved. PSCs with a stability extending up to one year have been realized, as documented by Roy *et al*. (2020). Several promising companies are now actively pursuing initiatives with the goal of introducing PSCs to the market.

Crucially, the IEC offers a vital industry benchmark for photovoltaic cells, delineated through the IEC 61215 standard. This standard encompasses a comprehensive suite of meticulous, time-intensive, and interconnected stress tests. Successfully attaining approval through these tests stands as a paramount and indispensable prerequisite for instilling confidence in consumers and investors, thereby charting the course toward commercialization. The IEC standard protocol systematically examines modules across diverse conditions. A multitude of tests are conducted to scrutinize their electrical and mechanical characteristics. Of utmost significance is the evaluation of environmental and operational stability (Mazumdar *et al*., 2021). It involves the following three steps:

i. Thermal cycling test-The module's resilience to thermal discrepancies, fatigue, and abrupt temperature variations is assessed. Thermal cycling spans from -40°C to 80°C, with a rapid heating/cooling rate of 100°C per hour. This cycle is repeated for a maximum of 200 cycles, each lasting no more than 6 hours, with a minimum dwell time of 10 minutes.

ii. Humidity-freeze test- Here a procedure is conducted to ascertain the module's capacity to endure the impact of elevated temperature and humidity, succeeded by exposure to low temperature. Initially, the module is exposed to 85°C and 85% relative humidity for 20 hours, after which it's rapidly frozen down to 0°C (with a maximum heating/cooling rate of 100°C per hour), followed by further cooling to -40°C for a duration of 4 hours. These steps can be iterated for a maximum of 10 cycles.

iii. Damp heat test - It is performed to assess the module performance over long time when exposed to humidity. It is examined under 85 ± 2°C temperature, 85 ± 5% RH for 1,000 h.

Only a few successful cases have been reported since IEC criteria require that PCE degradation must not go beyond 5% of initial PCE value recorded before the test, PSCs being more vulnerable to degradation.

CHAPTER THREE
MATERIALS AND METHODS

3.1 Materials

First and foremost, commercial FTO-coated glass substrate formed the foundational base for subsequent layers in the solar cell. Essential chemical components in this study included tin (IV) oxide, cesium (II) iodide, tin (II) iodide, and germanium. These were materials that were crucial for the desired perovskite structure. DMF and DMSO played integral roles in solution preparation and film processing, while copper acetate and ascorbic acid served as essential precursors in fabricating the HTL. Additionally, graphite powder was utilized in electrode fabrication, while chlorobenzene acted as a solvent for perovskite film formation. Deionized water was indispensable for cleaning and solution preparation throughout the synthesis process. Moreover, specialized equipment was employed, and they played vital roles; a magnetic stirrer aided in solution mixing, a sputtering machine facilitated ETL thin film deposition, a spin coater ensured uniform substrate coating of the perovskite and HTL layers and screen printing was used for graphite deposition.

3.2 Methodology

3.2.1 Cleaning of the FTO Substrates

The FTO substrates surfaces were wiped using clean residue free wipes dipped in acetone to remove any dust, dirt, fingerprint or any organic contaminant like grease and oil then further cleaned using ethanol. The substrates were then rinsed in deionized water to remove any residue that remained from the organic solvents. This was followed by drying them in a vacuum oven at 50°C to avoid possible damage to the FTO substrate coatings. They were then allowed to dry for 15 minutes, removed and stored in a dust free chamber.

3.2.2 Deposition of the SnO_2 ETL

The Edwards 360 Auto Sputtering Machine's vacuum chamber was cleaned thoroughly using ethanol. The cleaned FTO substrates were then placed on the substrate holder in the vacuum chamber and the SnO_2 target was loaded on the source. The chamber was closed and pumped down to a base pressure of 1.4 $x10^{-4}$ mbar. A current of 3.7 A was set for the achievement of 30 nm thickness thin film. The film was deposited onto the cleaned FTO substrate using the thermal evaporation method. This was followed by annealing them at 350°C for 30 minutes to allow sufficient crystallization so that the properties of the films may be improved. The procedure was repeated to deposit a second film with a thickness of 50 nm.

3.2.3 Synthesis and Deposition of $CsSnI_3$-Ge Absorber Layer

$CsSnI_3$-Ge solution was obtained by combining 0.65 g ± 0.01 g CsI, 0.93 g ± 0.01 g SnI_2 powders and a 5mole% Ge concentration which is equivalent to 0.036 g ± 0.001 g of Ge powder dissolved them in 15 ml DMF and DMSO mixed solution mixed at 1:2 ratio. The solution was stirred well for 15 minutes using a magnetic stirrer at 80°C. The solution was then spin coated onto three FTO glass substrates at different spinning speeds of 2000 rpm, 3000rpm and 4000rpm respectively for 60 s. A volume of 100 µL of an antisolvent chlorobenzene was then applied 20 s before the end of each spin cycle to enhance uniform crystallinity and crystal quality of the films. This was followed by drying of the films in a vacuum oven at 50°C for 15 minutes before annealing at 120°C for 30 minutes.

3.2.4 Characterization of the Thin Films

The optical properties of the SnO_2 and $CsSnI_3$-Ge thin films were measured using the Ossila USB Spectrometer. The structural properties $CsSnI_3$-Ge were obtained using a Rigaku Ultima IV X-ray diffractometer with Cu-Kα radiation (40 kV/ 44 mA) of wavelength λ = 1.5406 Å at an angle 2θ while their morphological SEM images were captured using a FEI Nova 200 Nano lab system scanning electron microscope under a 20,000 X magnification. An accelerating voltage of 5.00 kV and a beam current of 0.40 nA with a working distance (WD) of 5.0 -5.1 mm was used. The operating conditions for imaging remained consistent and constant for the three films.

3.2.5 Fabrication of the Solar Cell

An optimized layer thickness of SnO_2 was deposited on the FTO substrate via thermal evaporation to form the ETL, followed by annealing at 350°C. $CsSnI_3$-Ge perovskite layer was then deposited using spin coating method at an optimized speed of 4000 rpm. For the Cu_2O HTL synthesis, 2 g ± 0.0001 g of copper (II) acetate was dissolved in 20 ml of distilled water in a beaker. 2 g ± 0.0001 g of ascorbic acid was then dissolved in 20 ml of distilled water in another beaker. The solutions were stirred for 15 minutes until all solids dissolved. The ascorbic acid solution was slowly added to the copper (II) acetate solution while continuously stirring, this initiated the reduction process of copper (II) to copper (I) ions and the solution changed colour from blue to reddish brown. The resultant Cu_2O solution was then spin coated onto the optimal perovskite layer with a rotational speed of 3000 rpm for 45 s. This was followed by annealing of the film at 120°C for 30 minutes. Graphite paste was then applied on the Cu_2O film using screen printing technique to achieve graphite layer which acted as the back electrode. The PSC device structure is as displayed in Figure 3.1.

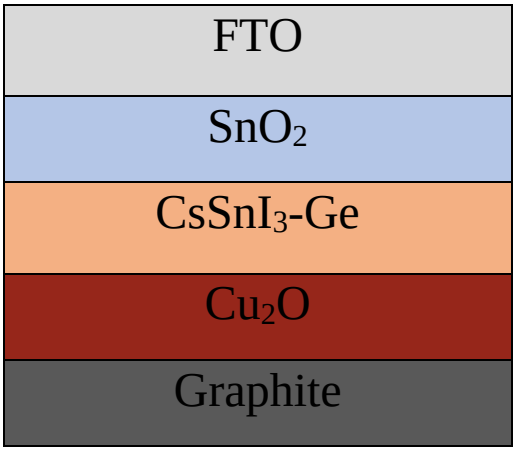

Figure 3.1: Structure of the PSC

3.2.6 Characterizing the Solar Cell

The electrical performance of the solar cell was recorded and evaluated using a SciSun-AM1.5G solar simulator with an illumination intensity of 100 $mWcm^{-2}$. All measurements and characterizations were recorded, evaluated and analyzed. Its FF was taken as the ratio of the product of the current at maximum power point (I_{mp}) and the voltage at maximum power point (V_{mp}) to that of the product of I_{sc} and V_{oc} (Dittrich & Thomas, 2015). It was calculated using the equation:

$$FF = \frac{I_{mp} \times V_{mp}}{I_{sc} \times V_{oc}} \quad (3.1)$$

Its efficiency (η) was taken as the ratio of the power output to that of the power of the sunlight (P_{sun}) illuminated on the solar cell (Dittrich & Thomas, 2015) and is given by the equation:

$$\eta = FF \frac{I_{sc} \times V_{oc}}{P_{sun}} \quad (3.2)$$

All the findings and discussions are presented in chapter four.

CHAPTER FOUR

RESULTS AND DISCUSSIONS

4.1 Optical Properties of SnO_2 Thin Films

Absorbance, transmittance and band gap are some of the optical properties of the SnO_2 thin film layers that were analysed. Graphs are used to present the findings, and they are well discussed in the next sections.

4.1.1 Transmittance of SnO_2 Thin Films

Figure 4.1 is a graphical representation of the optical transmission spectra of SnO_2 thin films as a function of wavelength in the range of 350 nm to 700 nm. The spectrum shows a trend whereby both film thicknesses display significant high transmittance across the visible spectrum, with values above 75% in the range of 500 nm to 700 nm. This is in agreement with a previous study of the SnO_2 thin films (Nwanna *et al*., 2022). This high level of transmittance is essential for SnO_2 used as ETL in PSCs, as it allows for efficient light absorption by the active layer beneath. This high transmittance of SnO_2 gives way for more sunlight to reach the perovskite absorber layer.

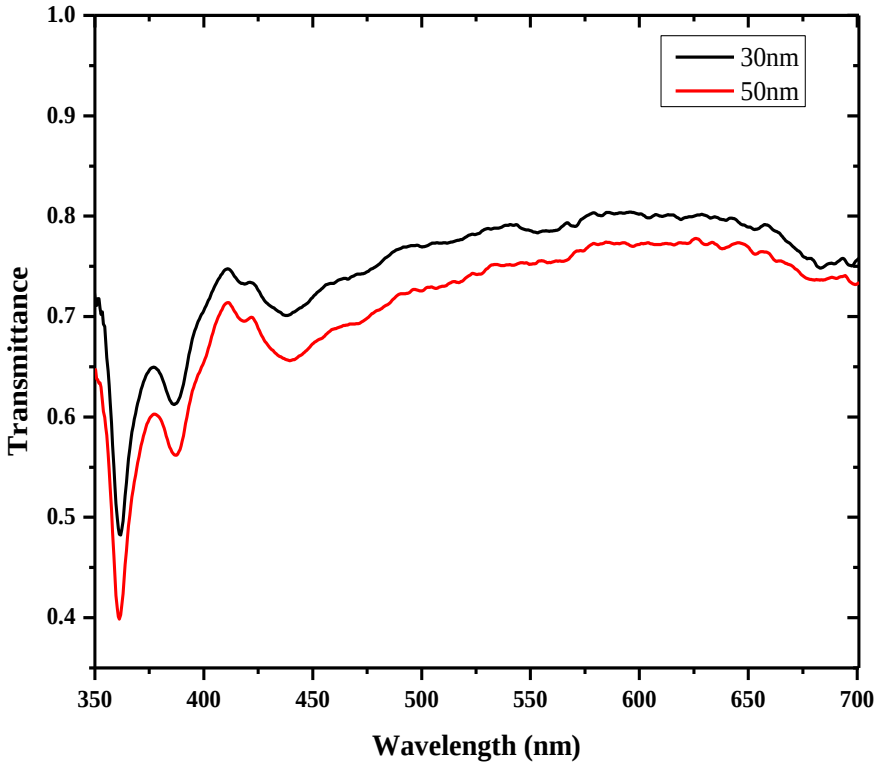

Figure 4.1: Variation of transmittance against wavelength for 30 nm and 50 nm thickness SnO_2 thin films

The 30 nm thickness layer displays a high transmittance of 80% whereas the 50 nm thickness film displayed a transmittance of 77% at a wavelength of about 614 nm. According

to Uysal e*t al*. (2015), the transmittance of SnO_2 is highly dependent on the grain size and surface morphology of the films. Therefore, this could mean that the thicker 50 nm layer has more grain boundaries. This could have contributed to light scattering losses within the film resulting in lower transmittance compared to the 30 nm thickness layer. From this study, it is probable that thinner films have high transmittance which allows more photons to reach the absorber layer. Therefore, the 30 nm thickness layer can be a suitable layer in environments where there is low light intensity since every photon counts.

4.1.2 Absorbance of the SnO_2 Thin Films

Figure 4.2 is a graphical representation of the optical absorbance of the SnO_2 thin films as a function of wavelength. Arslan *et al*. (2011) noted that the absorbance of SnO_2 films increases with an increase in the thickness of the films and they attributed this to scattering. In this study, the 30 nm thickness layer displays an absorbance of about 0.15 a.u whereas the 50 nm thickness layer displayed an absorbance of 0.18 a.u at a wavelength of about 438 nm. The 0.03 a.u difference could have resulted from the increase in thickness of the films which resulted to an increase in the size of the crystals and the surface roughness (Kuang *et al*., 2018). This could have resulted to an increase in scattering of light in the 50 nm thickness layer explaining the higher absorbance due to enhanced light trapping.

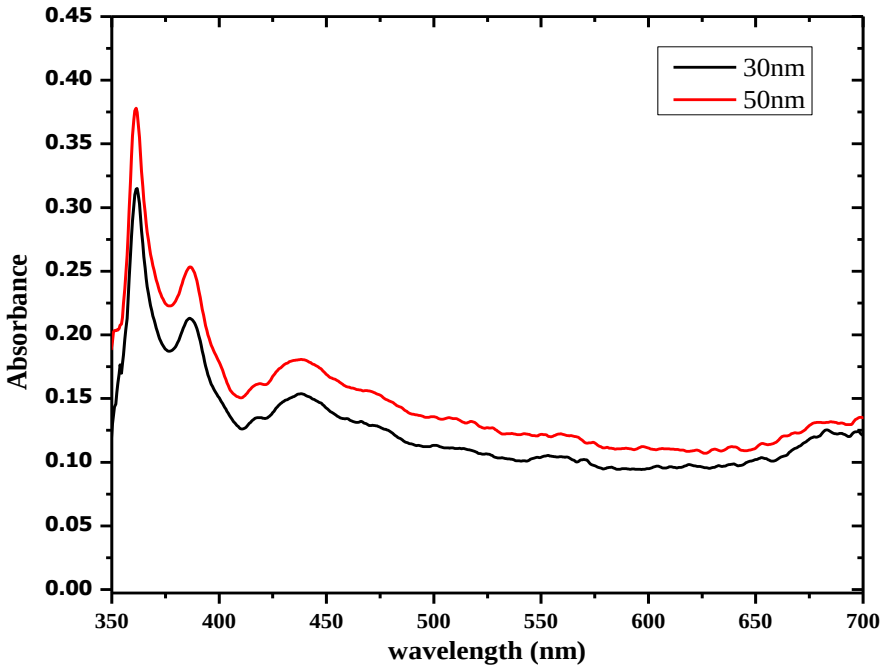

Figure 4.2: Variation of absorbance against wavelength for 30 nm and 50 nm thickness SnO_2 thin films

Absorption is noted to be higher at shorter wavelengths as compared to longer wavelengths in both layers. The strong absorption peaks appear at 361 nm and 386 nm. This

can be attributed to direct band transitions of electrons from the valence band to the conduction band in relation with the band gap energy of the material (Parves *et al*., 2020). This agrees with the theoretical relationship between wavelength (λ) and bang gap energies (Vasconcelos *et al*., 2024):

$$\lambda = \frac{hc}{E_g} \tag{4.1}$$

Where h is the Planck's constant, c the speed of light and E_g the band gap of the material. As a result, the strong absorption peaks observed at the specific wavelengths could correspond to the band gap energy of the material. Absorption is low in the visible light range with the 30 nm thickness film displaying lower absorbance as compared to the 50 nm thickness layer. This can confirm that increased thickness results in higher absorbance, as thicker films can absorb incident photons more efficiently than thinner ones. Therefore, the 30 nm film has the least absorbance and higher transmittance.

4.1.3 Band gap the SnO_2 Thin Films

The band gap of the material was determined via the Tauc plot using the Tauc relation:

$$(\alpha h\upsilon)^2 = A(h\upsilon - E_g) \tag{4.2}$$

where hυ is the photon energy, α the absorption coefficient and A the absorbance of the material. The α was calculated using the equation:

$$\alpha = 2.303 \times \frac{A}{L} \tag{4.3}$$

Where L is the known thickness of the thin film. A graph of $(\alpha h\upsilon)^2$ was plotted as a function of E_g as shown in Figure 4.3. Band gap was determined by extrapolating the linear region(s) of the curve. The value where the line intercepts the x-axis is the band gap value. This was determined to be between the range of 3.02 eV and 3.34 eV for both the 30 nm and 50 nm thickness layers. This agrees with a previous report which attained an optical band gap of 3.03-3.35 eV (Uysal *et al*., 2015).

Uysal *et al*. (2015) investigated SnO_2 nano films and found that the band gap value decreased with an increase in annealing temperature. Therefore, the slightly lower band gap determined in this study as compared to some literature values (3.6 eV to 4.0 eV) (Baena *et al*., 2015) can be attributed to possible quantum confinement effect resulting from subjecting the SnO_2 film to a high annealing temperature.

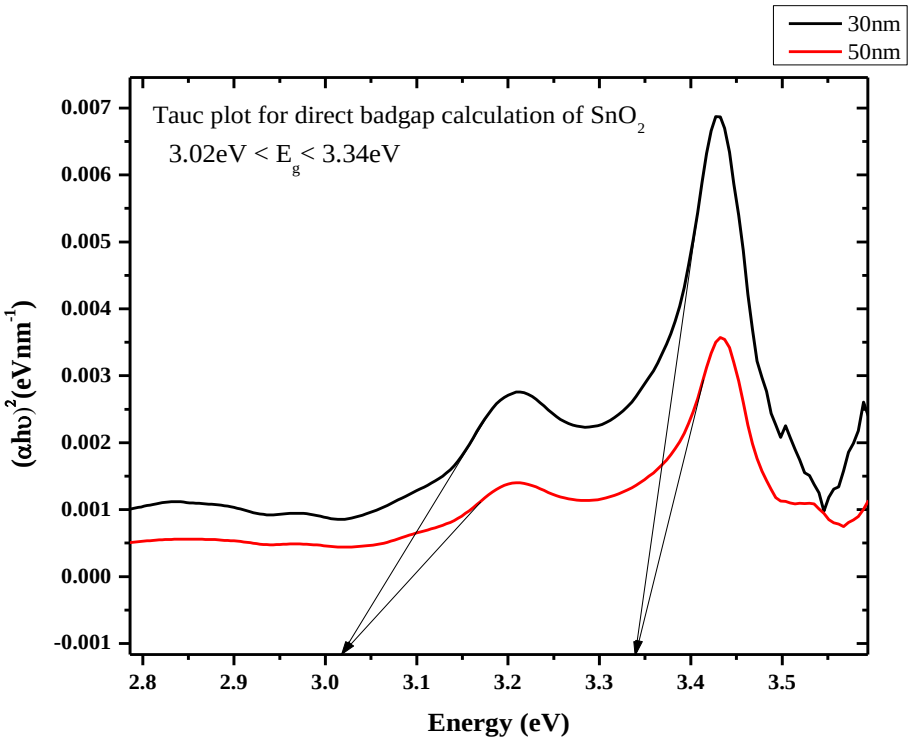

Figure 4.3: Tauc plot for direct band gap calculation of SnO_2 thin films

Both the 30 nm and 50 nm thickness films were annealed at a temperature of 350°C which is slightly higher than the recommended temperature of 200°C (Yang *et al.*,2018). High temperature (HT) annealed SnO_2 films have been reported to have a narrower band gap as compared to low temperature annealed SnO_2 films (Ke *et al.*, 2015). This might be due to the HT annealed SnO_2 having bigger nanoparticles as compared to the LT annealed SnO_2 films which resulted in the quantum confinement effect in HT annealed SnO_2 films. This could explain the narrower band gap. The band gaps for both layers lie in the same range and indicate that effects of thickness are not strong enough to significantly cause a change in the band gap energy. The deposition conditions in thermal evaporation remained consistent throughout possibly resulting in uniform deposition of both layers. This in turn forms similar crystal structures which could in turn result in a similar range of band gap values.

As much as the high temperature annealing improves the crystallinity of the films, it also has the potential of changing the morphology of the films and this can be further confirmed using SEM measurements. Hakeem *et al.* (2024) investigated different annealing temperatures of SnO_2 films ranging from 130°C to 180°C and concluded that the film treated at 150°C displayed enhanced optical and charge carrier properties. Therefore, in future studies, different annealing temperatures should be explored for optimal results.

4.2 Optical Properties of $CsSnI_3$-Ge Thin Films

The optical properties in this section were presented in the form of graphs and analysis followed. This was based on the concept that a material's photoconductivity depends on how much light energy is absorbed by the material (Hossain *et al.*, 2023). Therefore, absorptivity plays a major role in the generation of excitons which is crucial for electricity production.

4.2.1 Absorbance of CsSnI3-Ge Thin Films

Figures 4.4, 4.5, 4.6 and 4.7 are graphical representations of the absorbance in the $CsSnI_3$-Ge thin films as a function of wavelength. The figures show a strong absorption peak in the visible light spectrum for all the three samples and but drops above 500 nm wavelength. This trend is similar and is in close agreement with the absorption range of perovskites which is between 400-750nm and decreases above 600nm as displayed by Chen *et al.* (2015). One of the products from the possible Sn oxidation in the perovskite layer is SnI_4 and Leijtens *et al.* (2017) identified its unique absorption spectra. Their SnI_4 reference spectra corresponds with the spectra in this study with a sharp absorption peak at about 380 nm. This peak is consistent in all the figures and could suggest the presence of SnI_4 in all three films. In general, the absorbance spectrums displayed suggest that $CsSnI_3$-Ge perovskite is a good absorber of photons. Figure 4.4 represents the absorbance spectrum of the $CsSnI_3$-Ge perovskite deposited at a spin coating speed of 2000 rpm. As shown in the figure, absorbance is high at lower wavelengths between 350-450 nm then it drops (<0.2 a.u) at 450 nm and remains constant above 500 nm wavelength. The suspected yellow polymorph perovskite is said to mostly absorb light at shorter wavelengths (Nematov *et al.*, 2025) which can explain the high absorption peaks in the UV region.

The thin film deposited at a spin coating speed of 3000 rpm displays an almost similar absorbance spectrum as the 2000 rpm thin film as is seen in Figure 4.7. Absorbance is high at lower wavelengths of below 450 nm drops above 460 nm and remains nearly constant above 500 nm. However, both layers (2000 rpm, 3000 rpm thin films) successfully display absorbance of approximately 0.66 a.u in the visible light region. It was suggested that spin coating speed influences film thickness of the perovskite thin films (Yan *et al.*, 2018). Figure 4.6 displays the absorbance spectrum of $CsSnI_3$-Ge thin films deposited at a spin coating speed of 4000 rpm.

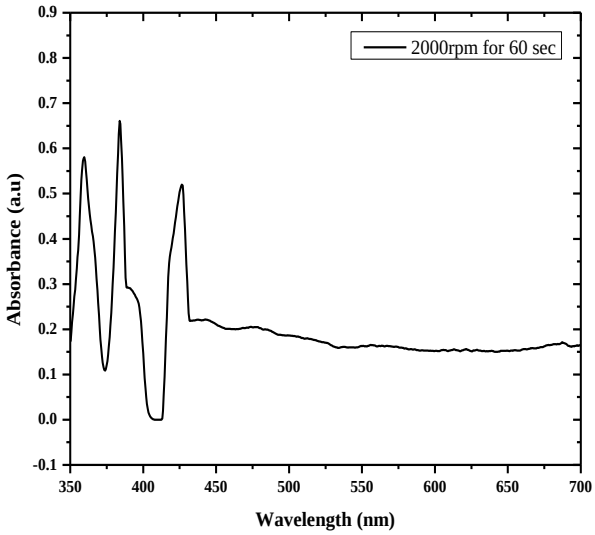

Figure 4.4: Absorbance spectra of $CsSnI_3$-Ge thin film deposited at a speed rotation of 2000 rpm

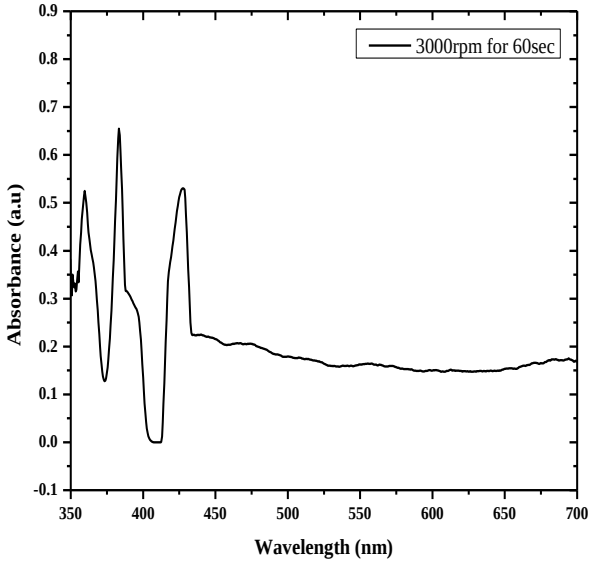

Figure 4.5: Absorbance spectra of $CsSnI_3$-Ge thin film deposited at a speed rotation of 3000 rpm

This film displays a high absorbance of approximately 0.77 a.u in the visible light region. There is an absorbance peak between 400- 450 nm range then it drops above 450 nm and remains constant above 500 nm (<0.3 a.u).

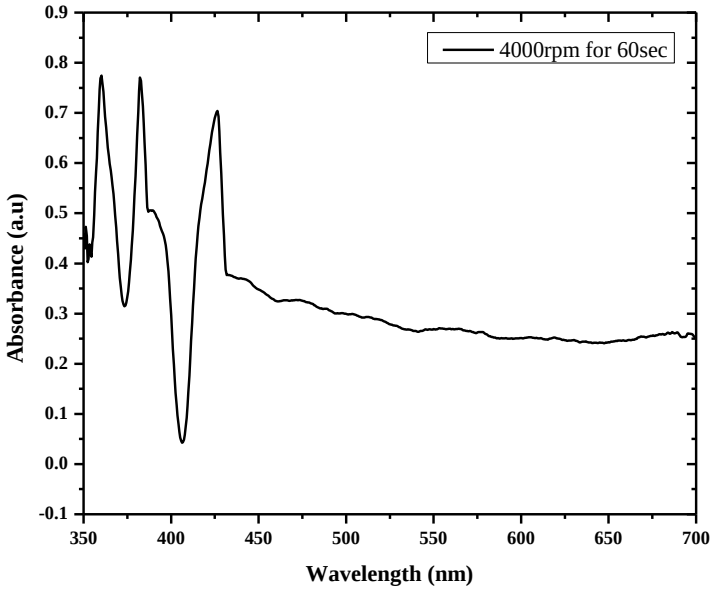

Figure 4.6: Absorbance spectra of $CsSnI_3$-Ge thin film deposited at a speed rotation of 4000 rpm

It has been shown that the absorbance of tin-based perovskites is easily influenced by the film thickness and the crystal quality of the perovskite (Wu *et al.*, 2021). These reasons could have resulted in peak intensities variations at different speeds as can be seen in Figure

4.7. The absorbance spectrum of the thin film resultant from 3000 rpm speed had a slightly lower absorbance though with a similar trend as the 2000 rpm counterpart thin film. It was suggested that the spin coating speed of 2000 rpm and 3000 rpm have negligible influence on variation of thickness in $CsSnI_3$-Ge thin film.

Comparing all three samples, it can be suggested that the layers produced at speeds of 2000 rpm and 3000 rpm display the lowest absorbance across the visible light spectrum because they formed thicker films due to lower speeds. The layers have a chance of suffering from scattering losses causing the low absorption (Yan *et al.*, 2018). It was also suggested that scattering losses may also be caused by the roughness and non-uniform surfaces of the resultant 2000 rpm and 3000 rpm speed layers as seen in the SEM images in Figure 4.10 and 4.11 respectively.

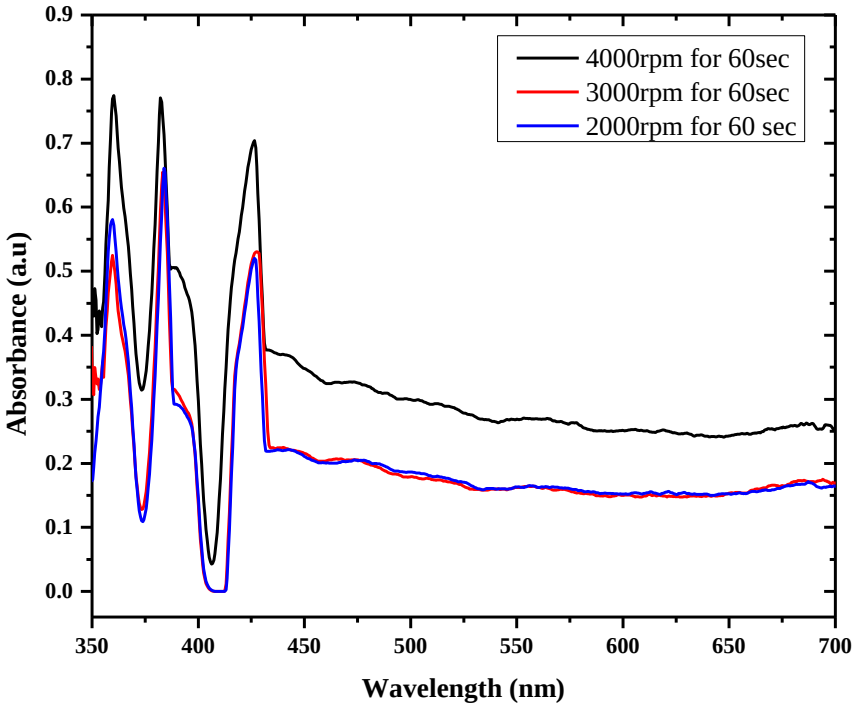

Figure 4.7: Absorbance spectra of $CsSnI_3$-Ge thin film deposited at different speed rotations: 2000 rpm, 3000 rpm and 4000 rpm

The thin film deposited at 4000 rpm speed displayed the highest absorbance as compared to the other two samples seen in Figure 4.7. Smoother films attract higher absorbance because there is enhanced light trapping as there is minimal light scattering at the surface of the film (Kumar *et al.*, 2023). This could explain the higher absorbance of the layer deposited at 4000 rpm speed since it may have a smoother and more uniform film compared to its counterparts. Therefore, higher speeds possibly result in thinner, smoother films. Perovskites are expected to be good absorbers of light hence the sample with the highest absorption is

preferred. In this study, the $CsSnI_3$-Ge thin film resulting from the 4000 rpm spin speed is ideal as it exhibited smooth morphology and is the highest absorber of photons.

4.2.2 Band gap of the $CsSnI_3$-Ge Thin Films

The band gap was determined via the Tauc plot using the Tauc relation in equation (4.2). The absorption coefficient was obtained using equation (4.4) where A is the absorbance

$$\alpha = 2.302 \text{ x A cm}^{-1} \quad (4.4)$$

of the material. A graph of $(\alpha h\upsilon)^2$ was plotted as a function of E_g as shown in Figure 4.8. The bandgap was determined by extrapolating the linear region(s) of the curve. The point where the lines intercepted the x-axis is the band gap.

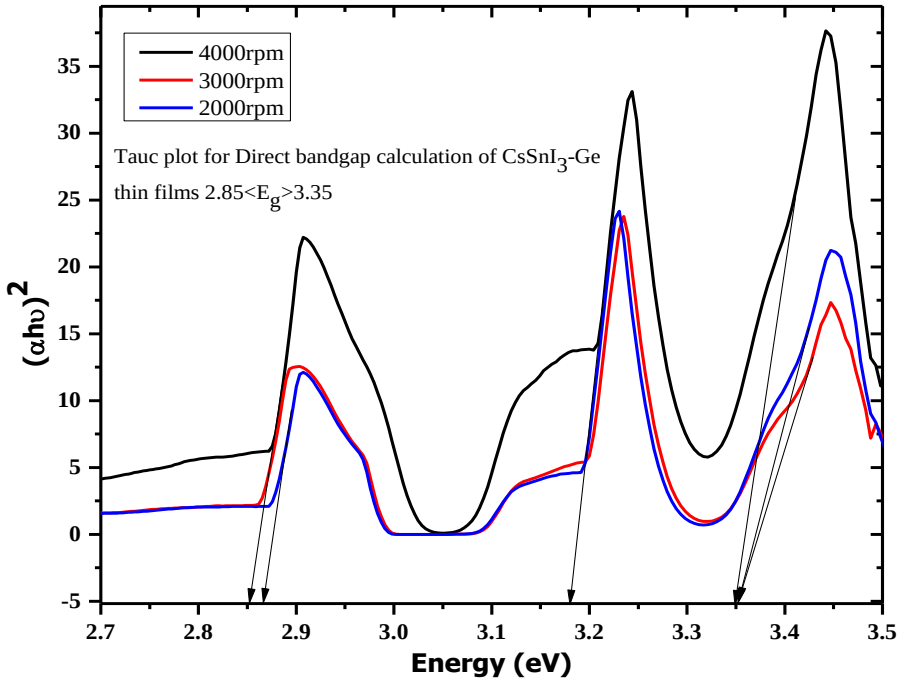

Figure 4.8: Tauc plot for direct band gap calculation of $CsSnI_3$-Ge thin films

Analysis suggested that all the films display almost similar band gap values that lie between 2.85 eV to 3.35 eV. These values are higher than the reported literature values at ~ 1.5 eV (Chen *et al*., 2019). This higher band gap value was attributed to the partial doping with Ge which may have not fully dissolved in the DMF/DMSO solution. This may have caused the native oxidation of Sn^{2+} vacancies to Sn^{4+} leading to the generation of Ge rich regions forming *p*-type orientations. This observation suggested that the investigated spin coating speeds had no serious influence or impact on the band gap of the $CsSnI_3$-Ge thin films. The ideal band gap for most single-junction solar cells for optimum solar cell performance is 1.35 eV (Buonassisi & Peters, 2018). However, the band gap can be easily tuned by adjusting other parameters like

doping and temperature during deposition. Tin trihalide perovskites are also known to have large band gaps which in turn lead to a low absorption capacity (Nematov *et al*., 2025).

Yellow phase compounds are characterized by large band gaps which could be the reason behind the huge band gap range (2.85 eV to 3.35 eV) for the perovskite in this study. This is in close agreement with the reported band gap value of 2.99 eV of yellow orthorhombic $CsSnI_3$ perovskite phase, indicating that the structure could have undergone phase transition at some point (Nematov *et al*., 2025). $CsSnI_3$ can also completely convert into a non-perovskite phase, Cs_2SnI_6 under storage in air for short periods of 48 hours or less which is also yellow in color (Qiu *et al*., 2017) making this another possible reason for the wider band gap in this study. However, the band gap of Cs_2SnI_6 is 1.46 eV which is narrower than the value in this study further suggesting the presence of a yellow orthorhombic $CsSnI_3$ phase here.

4.3 Structural Analysis of $CsSnI_3$-Ge Thin Films

Figure 4.9 is an XRD pattern of the three samples deposited at different spin coating speeds of 2000 rpm, 3000 rpm and 4000 rpm. The successful synthesis of the perovskite structures was confirmed by the sharp peaks which correspond to specific planes in the crystal structures. Higher peaks are as a result of a greater degree of crystallinity and the sharpness of the peaks can also indicate the crystallinity degree. Nearly all the peaks from the samples at different spin speeds of 2000 rpm, 3000 rpm and 4000 rpm have similar diffraction planes indicating that they might all have a similar crystalline phase. This shows that the change in spin coating speeds did not alter the crystal structure of the perovskite.

$CsSnI_3$ is a unique phase change perovskite and can exist in four polymorphic phases including the black tetragonal (Bβ), black cubic (Bα), black orthorhombic (Bγ) and yellow orthorhombic (Yγ). On air exposure, the Bγ phase can change to the Yγ phase due to the oxidation of Sn (Chung *et al*., 2012). Peaks of about 27° and 29°are known to correspond to Bγ $CsSnI_3$ phase of the (202) plane (Minj *et al*., 2023) therefore, in this study the 26.5° peak angle could suggest the presence of $CsSnI_3$ perovskite. However, only three of the characteristic peak angles reported for the Bγ $CsSnI_3$ (Howlader *et al*., 2022) match the peak angles in this study which could suggest the presence of a different phase. It can be reported that the observed XRD patterns for all the three thin films synthesized at different spin coating speeds seen in Figure 4.9 are in good agreement with the reported orthorhombic structure of yellow $CsSnI_3$ (Zhang *et al*., 2014). They also found that the Yγ $CsSnI_3$ polymorph is the most stable at room temperature when exposed to organic solvents as compared to the Bγ $CsSnI_3$ polymorph. This also corresponds to the suspected Yγ structure determined during band gap calculation in section 4.2.2.

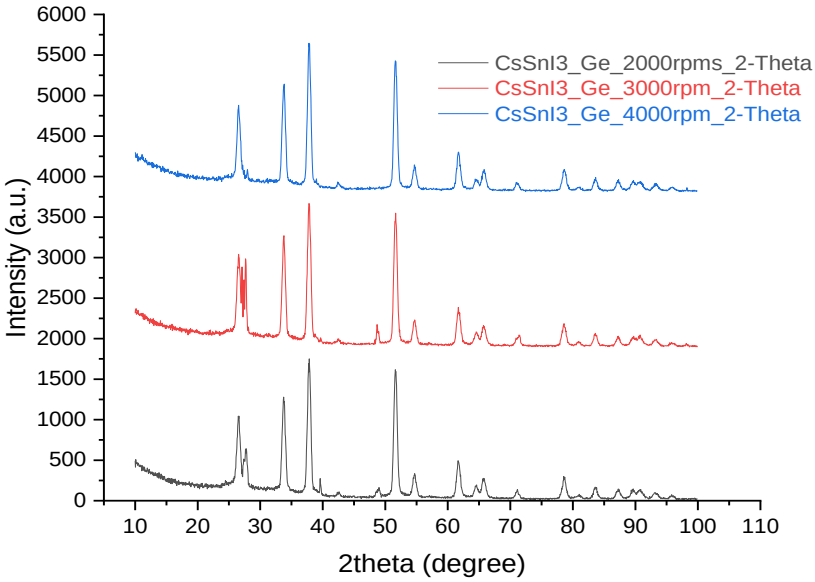

Figure 4.9: XRD patterns of the $CsSnI_3$-Ge thin films deposited on FTO glass substrates at different speed rotation: 2000 rpm, 3000 rpm and 4000 rpm

The reported characteristic peaks of CsI and SnI_2 are about 12.8° and 27.6° respectively (Zhu *et al*., 2018). In this study, there is a high intensity peak at 26.5° which is close to 27.6°. This could mean that there was an excess of SnI_2 residue due to the incomplete solubility of Ge where a complete reaction with SnI_2 was expected. On the other hand, the existence of no peak at around 12.8° could mean that there were no residues left of CsI. The additional short peaks could suggest the presence of other phases according to Sutton *et al*. (2018). Nearly all the peaks from the samples at different spin coating speeds of 2000 rpm, 3000 rpm and 4000 rpm have similar intensities with the 4000 rpm thin film displaying slightly higher intensity peaks. Higher intensity peaks correspond to better/higher crystallinity which is preferred because device stability is highly dependent on the crystallinity of the perovskite layer (Fakharuddin *et al.*, 2015). Higher crystallinity of the perovskite can also lead to minimized defects state and charge recombination hence an improved device efficiency (Seyed-Talebi *et al*., 2021). It can be concluded that higher speeds promote crystal growth as seen from the increased intensity of the peaks with an increase in spin coating speeds.

4.4 Morphological Analysis of $CsSnI_3$-Ge Thin Films

Figures 4.10, 4.11 and 4.12 display the morphological analysis of the samples taken at a 20,000 X magnification. The film crystals and sizes are equally and evenly distributed. All the three top view SEM images displayed rhombic shaped crystallites and did not display a significant difference in crystal size. It was suggested that due to the incomplete solubility of Ge particles, the resultant dopant free $CsSnI_3$ perovskite phase underwent oxidation during

crystallization from Sn^{2+} to Sn^{4+} leading to the incomplete surface coverage (Liu *et al*., 2020). This could explain the physical nature of the images. The SEM images for the three samples were found to have slightly different morphologies which is evidence that spin coating speed affects the morphology of thin films.

Figure 4.10: $CsSnI_3$-Ge at 2000 rpm speed

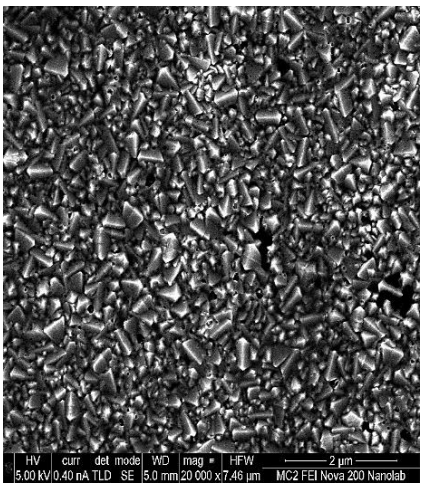

Figure 4.11: $CsSnI_3$-Ge at 3000 rpm speed

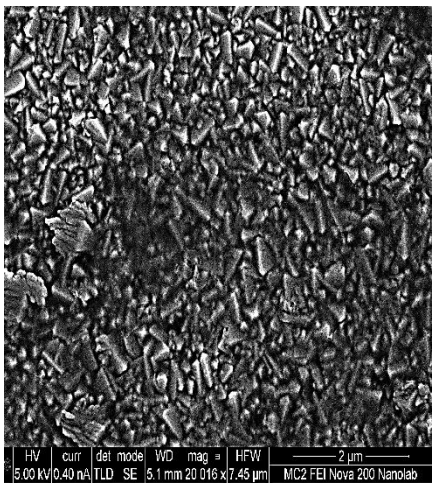

Figure 4.12: $CsSnI_3$-Ge at 4000 rpm speed

From Figure 4.11, the 2000 rpm layer appears to have a more incomplete surface coverage with layer grains. The surface also appears to be relatively rough and is likely thicker making it prone to agglomeration. From Figure 4.12 generated from a speed of 3000 rpm, the surface of the layer appears slightly smoother and more compact as compared to the surface of the film deposited at a speed of 2000 rpm. Its crystals seem to be more refined with fewer visible gaps. This could have been due to the increased centrifugal force which ensured effective and uniform distribution of the solution on a surface due to the rapid spread. This also results in the formation of a thinner film which agrees with literature findings (Yan *et al*., 2018) that higher speeds result to thinner films (Avinash & Mendhe, 2023). However, some regions in this layer show particle agglomeration with visible irregularly distributed large clusters as seen in Figure 4.11.

Figure 4.12 represents the image obtained from the highest spin coating speed at 4000 rpm. Its surface appears more uniform as compared to those in Figure 4.11 and 4.12. The higher 4000 rpm speed in this study is likely to produce a much more uniform film as a result of faster nucleation and crystallization associated with high spinning speeds (Osman *et al.,* 2024). The surface could appear smoother with less visible grain boundaries. Higher speed causes rapid solvent removal and good distribution of particles on the surface. In solar cells, smother surfaces enhance charge transport and end up reducing charge recombination by minimizing

the leakage current (Qu *et al.,* 2024). Therefore, it is critical to achieve a smooth perovskite surface. A uniform surface coverage with large grain sizes could lead to a higher efficiency in a fabricated solar cell as this may reduce recombination at its grain boundaries (Samanta *et al.,* 2024). Among the three samples highlighted in this study, the 4000 rpm layer was the optimal layer as it displayed a smoother surface.

4.5 I-V Characterization of the Fabricated Solar Cell

Table 4.1 displays the device parameters of three fabricated solar cell devices. In this table, the values of J_{sc} were influenced by the electric field in the solar cell. This electric field is influenced by the charge generation, charge extraction efficiency and charge transport. Figure 4.14 shows the J-V characteristics curve of the fabricated solar cell from the optimized conditions and films. Among the three solar cells, the highest overall efficiency of 2.458 %, with V_{oc} of 0.7056 V, a J_{sc} of 8.868 mA.cm^{-2}, a FF of 39.27% and a maximum power point (P_{MP}) of 0.002458 W was achieved by device 3. These values were computed using equation (3.1) and equation (3.2) as:

$$FF = \frac{2.458 \text{ x } 10^3}{8.868 \text{ x } 0.7056 \text{ x } 10^3} = 39.27\% \quad (4.5)$$

$$\eta = 39.27 \frac{8.868 \text{ x } 0.7056 \text{ x } 10^3}{100} = 2.458\% \quad (4.6)$$

Table 4.1: J-V Characteristics of the Fabricated PSCs Device**s**

Device Parameters	**PCE (%)**	**FF (%)**	**J_{sc} (mA.cm^{-2})**	**V_{oc} (V)**	**MP (W) (x10^{-3})**	**R_{shunt} (Ohm.cm^2)**	**R_{series} (Ohm.cm^2)**
Device 1	1.81670	32.96079	-10.17512	0.54168	-1.81670	76.66692	29.57000
Device 2	1.91693	34.02793	-11.24277	0.50107	-1.91693	69.28016	33.00836
Device 3	2.45750	39.27140	-8.86846	0.70562	-2.45750	337.81998	41.72689

Maximum absorbance is preferred for a perovskite absorber however, the highest achieved absorbance was approximately 77%. This meant that the projected efficiency could not be achieved as this slightly lower absorbance led to a lower charge generation. The lower photon absorption by the perovskite layer shown in Figure (4.7) in section (4.2.1) in turn resulted in low J_{sc} values of about 8.868 mA.cm^{-2}. The low value of J_{sc} can also be attributed to the thick nonuniform graphite layer observed in this study which acts as a barrier in charge extraction with several defects (Meng *et al.,* 2024). Some of the factors that affect V_{oc} are the

rate of charge carrier recombination and the energy level alignment of the photoactive layers. The reported V_{oc} of 0.7056V agrees with the results of other inorganic Sn^{2+} based perovskites (Song *et al.,* 2017). This high V_{oc} can be attributed to the good energy level alignment between the ETL and the perovskite layer which reduces charge carrier recombination at interfaces and minimizes energy loss (Yu *et al.,* 2023).

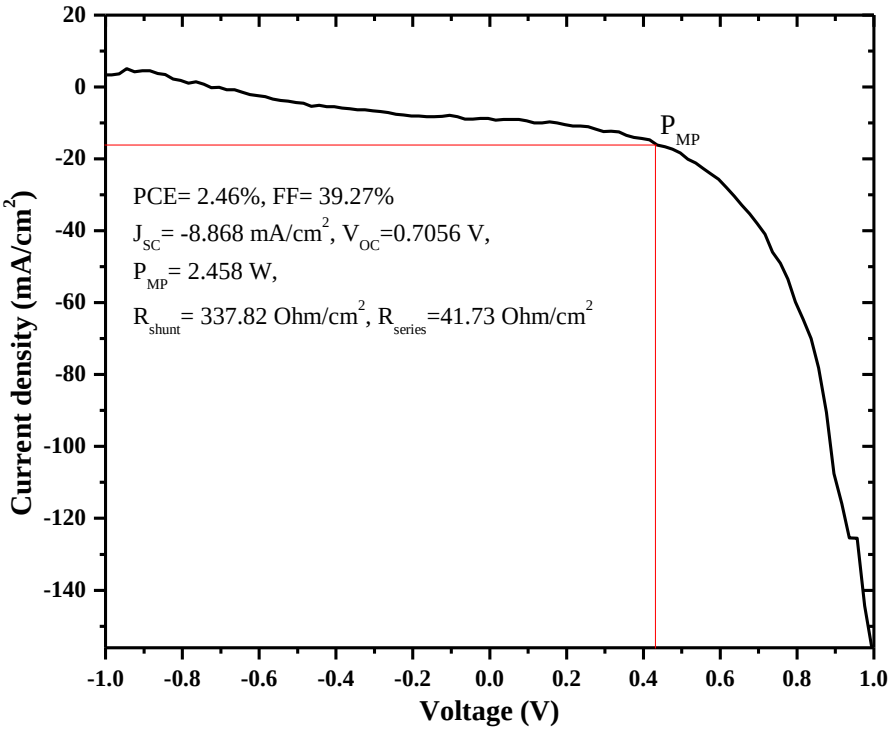

Figure 4.14: J-V Characteristics curve of the fabricated solar cell

In this PSC, the current density is lower, but the V_{oc} is high suggesting a reduction in recombination losses with well aligned energy levels of the photoactive layers. The optimal perovskite film suggested good crystallinity and uniform surface coverage as seen from the SEM and XRD results. This could have led to the higher V_{oc} and R_{shunt} of 337.82 Ohm.cm^2. The undissolved Ge which settled at the bottom of the beaker, did not completely substitute the Sn^{2+} vacancies in the perovskite solution causing their oxidation to Sn^{4+}. Presence of Sn^{4+} is one of the limiting factors of Sn based PSCs which could cause the shorting of devices originating from the metallic like highly doped *p*type materials. Hence, the low FF can be attributed to the high number of Sn^{4+} present in the films due to the Sn^{2+} oxidation (Yokoyama *et al.,* 2017). The partial solubility of Ge is the suggested reason behind the inconsistent performance of the three solar cells despite a similar fabrication procedure. Due to the possible uneven Ge doping, some regions of the film could have experienced better charge transport while others experienced recombination explaining the difference in the data values.

Higher R_{series} and lower R_{sh} lead to lower photocurrent as a result lowering the efficiency of the solar cell (Mehde *et al*., 2020) therefore, a higher R_{sh} and low R_{series} are preferred. Device 3 which is the best performing solar cell, has the highest R_{sh} of 337.82 Ohm.cm^2 and the R_{series} is reasonably slightly high at 41.73 Ohm.cm^2. The high R_{series} could be due to an increase in grain boundary resistance causing charge recombination and in turn reducing the efficiency of the cell, explaining the low efficiency of 2.458%. This is because Ge may not have been fully incorporated into the lattice of the perovskite. The high R_{series} can also be due to the graphite layer electrode applied via the screen-printing technique as the layer appeared slightly thick and could lead to poor charge transport. This solar cell device has a high R_{sh} which is good agreement with literature values and is suitable for a working solar cell. The FF of a device is dependant on the material quality and is improved with high R_{sh} as leakage currents are suppressed (Mortadi *et al*., 2024).

In this study, the excessive p-type doping of Sn^{2+} to Sn^{4+} in the perovskite layer creates leakage pathways which could explain the low FF (Xiong *et al*., 2024). The high R_{series} could also have led to the low FF because of the inefficient extraction of charges and their transportation (Wang *et al*., 2024). Therefore, an increase in FF can lead to an improvement in PCE. The low PCE recorded could also be because of the high density of defects arising from *p*type dopants present in the perovskite layer. Additionally, the large band gap of the perovskite layer could have contributed to an increase in the V_{oc} but reduced J_{sc} and ultimately the overall affecting device efficiency. Fabrication conditions, charge carrier recombination, reduced photon absorption, perovskite film quality and the graphite electrode thickness potentially contributed to the PSC's low PCE.

CHAPTER FIVE

SUMMARY, CONCLUSIONS AND RECOMMENDATIONS

5.1 Summary

Solar energy has been preferred in this study due to its vast availability and abundance. Third generation PSCs have proven to be highly efficient, cost effective and can be fabricated using simple techniques. As a result, this research successfully investigated lead free $CsSnI_3$-Ge based PSCs to ensure sustainability and potential efficiency improvement. First, the SnO_2 ETL was thermally evaporated on FTO glass substrates using a sputtering machine. Two thin films of 30nm and 50nm thicknesses were deposited and annealed and their optical properties investigated using a UV-Vis spectrophotometer. High transmittance was expected for this layer to allow maximum penetration of light to the perovskite layer.

Spin coating method was used to deposit the $CsSnI_3$-Ge perovskite solution on three FTO glass substrates at different spin coating speeds of 2000 rpm, 3000 rpm and 4000 rpm. The films were then dried and annealed, and their optical, structural and morphological analysis done using UV-Vis spectrophotometer, XRD and SEM machines respectively. From the characterization results, optimal parameters were chosen for the fabrication of a PSC of structure FTO/SnO_2/$CsSnI_3$-Ge/ Cu_2O/ C. Three devices were fabricated and their photovoltaic parameters, that is the FF, J_{sc}, V_{oc} and PCE investigated.

This study highlighted the influence of thickness variation of the SnO_2 ETL on its optical properties. The effect of speed coating speed variation on the optical, structural and morphological properties of $CsSnI_3$-Ge perovskite was also studied for optimum solar cell performance. These in turn affected the general performance of the fabricated solar cells. From analysis, the following conclusions were drawn.

5.2 Conclusions

i. The transmission spectrum of all the SnO_2 ETLs displayed high transparency in the visible light region. The absorbance/transmittance data confirms that increased thickness results in higher absorbance and lower transmittance making the 30 nm thickness layer the optimal layer for fabrication in this study. The band gap value for both layers were slightly lower than reported values possibly due to the high annealing temperatures at 350°C. However, the determined band gap range is still favorable for solar cell applications. Their high transparency also makes SnO_2 thin films a potential ETL in PSCs fabrication.

ii. The $CsSnI_3$-Ge layer deposited at a spin coating speed of 4000 rpm displayed the highest absorbance. The band gap of the films is in the range of 2.85 eV to 3.35 eV

which is higher than the ideal value of ~1.5 eV. This is attributed to the incomplete Ge incorporation into the $CsSnI_3$ perovskite which leads to phase inconsistencies due to oxidation. The $CsSnI_3$-Ge thin films however exhibited good optical properties in the visible light spectrum. This makes it a suitable absorber layer in photovoltaic applications.

iii. The XRD analysis revealed the presence of an orthorhombic phase which is common with perovskite materials. The $CsSnI_3$-Ge layers display high intensity peaks corresponding to good crystallinity. The morphological analysis of the $CsSnI_3$-Ge films shows incomplete surface coverage. However, the surface of the 4000 rpm layer appears smoother and more uniform, suggesting that higher speeds result in smoother, more uniform thin films. Smoother films contribute to the efficiency of a solar cell making it a favorable layer in PSC fabrication.

iv. The optimal layer parameters resulted in a PSC with a PCE of 2.458% an V_{oc} of 0.7056 V, a J_{sc} of 8.868 $mA.cm^{-2}$ and a FF of 39.27%. This output is still low but agrees with that of several Sn based PSCs. These results can be referenced by researchers in future enhancement and development of PSCs. As a result, the outcomes of this study will help contribute to advancements in renewable energy technologies, research and promotion of sustainable energy solutions.

5.3 Recommendations

i. The annealing temperatures of SnO_2 ETL should be investigated to achieve an optimal temperature that does not reduce the band gap value ensuring the maximum performance of the charge transport layer.

ii. Alternative synthesis routes for Ge doping should also be explored to attain an ideal band gap value for maximum absorption.

iii. An inert atmosphere or an all-vacuum environment is recommended for the synthesis of Sn based perovskites. This is to prevent the rapid native oxidation of Sn^{2+}, in turn minimizing the phase inconsistencies.

iv. Future research should aim at improving the FF of the device by targeting lower R_{series} and higher R_{shunt}. The charge concentration values can then be determined from hall effect measurements. Additionally, interface and surface passivation strategies should be considered for an improved V_{oc} which will in turn lead to a higher PCE.

REFERENCES

Abas, N., Kalair, A., & Khan, N. (2015). Review of fossil fuels and future energy technologies. *Futures, 69*, 31-49.

Aftab, A., & Ahmad, M. I. (2021). A review of stability and progress in tin halide perovskite solar cell. *Solar Energy*, *216*, 26-47.

Al-Ghamdi, S. N., Al-Ghamdi, H. A., El-Shishtawy, R. M., & Asiri, A. M. (2021). Advances in phenothiazine and phenoxazine-based electron donors for organic dye-sensitized solar cells. *Dyes and Pigments, 194*, 109638.

Babayigit, A., Ethirajan, A., Muller, M., & Conings, B. (2016). Toxicity of organometal halide perovskite solar cells. *Nature materials*, *15*(3), 247-251.

Baena, J. P. C., Steier, L., Tress, W., Saliba, M., Neutzner, S., Matsui, T., ... & Hagfeldt, A. (2015). Highly efficient planar perovskite solar cells through band alignment engineering. *Energy & Environmental Science*, *8*(10), 2928-2934.

Boro, B., Porwal, S., Kumar, D., Mishra, S., Ghosh, S., Kansal, S., ... & Singh, T. (2022). Perovskite Solar Cells: Assessment of the Materials, Efficiency, and Stability. *Catalysis Research*, *2*(4), 1-48.

Cao, J., You, P., Tang, G., & Yan, F. (2023). Two-dimensional materials for boosting the performance of perovskite solar cells: Fundamentals, materials and devices. *Materials Science and Engineering: R: Reports*, *153*, 100727.

Cao, X., Hao, L., Liu, Z., Su, G., He, X., Zeng, Q., & Wei, J. (2022). All green solvent engineering of organic–inorganic hybrid perovskite layer for high-performance solar cells. *Chemical Engineering Journal*, *437*, 135458.

Cao, X., Zhi, L., Jia, Y., Li, Y., Zhao, K., Cui, X., ... & Wei, J. (2019). A review of the role of solvents in formation of high-quality solution-processed perovskite films. *ACS applied materials & interfaces*, *11*(8), 7639-7654.

Chapin, D. M., Fuller, C. S., & Pearson, G. L. (1954). A new silicon p-n junction photocell for converting solar radiation into electrical power. *Journal of applied physics*, *25*(5), 676.

Chen, J. K., Zhang, B. B., Liu, Q., Shirahata, N., Mohammed, O. F., Bakr, O. M., & Sun, H. T. (2021). Advances and challenges in tin halide perovskite nanocrystals. *ACS Materials Letters*, *3*(11), 1541-1557.

Chen, J., Cai, X., Yang, D., Song, D., Wang, J., Jiang, J., ... & Ni, C. (2017). Recent progress in stabilizing hybrid perovskites for solar cell applications. *Journal of Power Sources*, *355*, 98-133.

Chen, L. C., Chen, J. C., Chen, C. C., & Wu, C. G. (2015). Fabrication and properties of high-efficiency perovskite/PCBM organic solar cells. *Nanoscale research letters*, *10*, 1-5.

Chen, M., Ju, M. G., Garces, H. F., Carl, A. D., Ono, L. K., Hawash, Z., ... & Padture, N. P. (2019). Highly stable and efficient all-inorganic lead-free perovskite solar cells with native-oxide passivation. *Nature communications*, *10*(1), 16.

Chen, R., Zhang, W., Guan, X., Raza, H., Zhang, S., Zhang, Y., ... & Chen, W. (2022). Rear electrode materials for perovskite solar cells. *Advanced Functional Materials*, *32*(26), 2200651.

Cheng, Y., So, F., & Tsang, S. W. (2019). Progress in air-processed perovskite solar cells: from crystallization to photovoltaic performance. *Materials Horizons*, *6*(8), 1611-1624.

Chiara, R., Morana, M., & Malavasi, L. (2021). Germanium-based halide perovskites: materials, properties, and applications. *ChemPlusChem*, *86*(6), 879-888.

Chowdhury, T. H., Reo, Y., Yusoff, A. R. B. M., & Noh, Y. Y. (2022). Sn-Based Perovskite Halides for Electronic Devices. *Advanced Science*, *9*(33), 2203749.

Chung, I., Song, J. H., Im, J., Androulakis, J., Malliakas, C. D., Li, H., ... & Kanatzidis, M. G. (2012). CsSnI3: semiconductor or metal? High electrical conductivity and strong near-infrared photoluminescence from a single material. High hole mobility and phase-transitions. *Journal of the american chemical society*, *134*(20), 8579-8587.

de Ménorval, M. A., Mir, L. M., Fernández, M. L., & Reigada, R. (2012). Effects of dimethyl sulfoxide in cholesterol-containing lipid membranes: a comparative study of experiments in silico and with cells. *PloS one*, *7*(7), e41733.

Dittrich, T. (2015). *Materials concepts for solar cells*. World Scientific.

Dixit, H., Boro, B., Ghosh, S., Paul, M., Kumar, A., & Singh, T. (2022). Assessment of lead-free tin halide perovskite solar cells using J–V hysteresis. *Physica status solidi (a)*, *219*(11), 2100823.

Dixit, H., Boro, B., Ghosh, S., Paul, M., Kumar, A., & Singh, T. (2022). Assessment of lead-free tin halide perovskite solar cells using J–V hysteresis. *Physica status solidi (a)*, *219*(11), 2100823.

Dubey, A., Adhikari, N., Mabrouk, S., Wu, F., Chen, K., Yang, S., & Qiao, Q. (2018). A strategic review on processing routes towards highly efficient perovskite solar cells. *Journal of Materials Chemistry A*, *6*(6), 2406-2431.

Eperon, G. E., Burlakov, V. M., Docampo, P., Goriely, A., & Snaith, H. J. (2014). Morphological control for high performance, solution-processed planar heterojunction perovskite solar cells. *Advanced functional materials*, *24*(1), 151-157.

Fagiolari, L., & Bella, F. (2019). Carbon-based materials for stable, cheaper and large-scale processable perovskite solar cells. *Energy & Environmental Science*, *12*(12), 3437-3472.

Fakharuddin, A., Di Giacomo, F., Ahmed, I., Wali, Q., Brown, T. M., & Jose, R. (2015). Role of morphology and crystallinity of nanorod and planar electron transport layers on the performance and long-term durability of perovskite solar cells. *Journal of Power Sources*, *283*, 61-67.

Ghadiri, M., Kang, A. K., & Gorji, N. E. (2020). XRD characterization of graphene-contacted perovskite solar cells: Moisture degradation and dark-resting recovery. *Superlattices and Microstructures*, *146*, 106677.

Gribkova, O. L., Kabanova, V. A., Tameev, A. R., & Nekrasov, A. A. (2019). Ink-jet printing of polyaniline layers for perovskite solar cells. *Technical Physics Letters*, *45*, 858-861.

Guo, F., Lu, Z., Mohanty, D., Wang, T., Bhat, I. B., Zhang, S., ... & Lu, T. M. (2017). A two-step dry process for Cs2SnI6 perovskite thin film. *Materials Research Letters*, *5*(8), 540-546.

Hakeem, S., Ali, S., Liaqat, M. A., Jamshed, A., Basit, M., Masood, M. T., & Javed, S. (2024). Effect of Annealing Temperature on the Morphology, Structure and Optical Properties of Spin-Coated SnO2 Films for Solar Cell Application. *Materials Proceedings*, *17*(1), 28.

Hoke, E. T., Slotcavage, D. J., Dohner, E. R., Bowring, A. R., Karunadasa, H. I., & McGehee, M. D. (2015). Reversible photo-induced trap formation in mixed-halide hybrid perovskites for photovoltaics. *Chemical Science*, *6*(1), 613-617.

Hossain, M. K., Ishraque Toki, G. F., Samajdar, D. P., Rubel, M. H. K., Mushtaq, M., Islam, M. R., ... & Madan, J. (2023). Photovoltaic performance investigation of $Cs_3Bi_2I_9$-based perovskite solar cells with various charge transport channels using DFT and SCAPS-1D frameworks. *Energy & Fuels*, *37*(10), 7380-7400.

Hossain, M. K., Toki, G. I., Kuddus, A., Rubel, M. H. K., Hossain, M. M., Bencherif, H., ... & Mushtaq, M. (2023). An extensive study on multiple ETL and HTL layers to design and simulation of high-performance lead-free $CsSnCl_3$-based perovskite solar cells. *Scientific Reports*, *13*(1), 2521.

Howlader, A. H., Li, F., & Zheng, R. (2022). Nanorod-like nanocrystalline $CsSnI_3$ and CNT composite thin film–based hybrid photodetector. *Emergent Materials*, *5*(6), 1925-1943.

Iqbal, J., Howari, F. M., Mohamed, A. M. O., & Paleologos, E. K. (2021). Assessment of radiation pollution from nuclear power plants. In *Pollution assessment for sustainable practices in applied sciences and engineering* (pp. 1027-1053). Butterworth-Heinemann.

Jena, A. K., Kulkarni, A., & Miyasaka, T. (2019). Halide perovskite photovoltaics: background, status, and future prospects. *Chemical reviews*, *119*(5), 3036-3103.

Jiang, X., Li, H., Zhou, Q., Wei, Q., Wei, M., Jiang, L., ... & Ning, Z. (2021). One-step synthesis of SnI_2·(DMSO) x adducts for high-performance tin perovskite solar cells. *Journal of the American Chemical Society*, *143*(29), 10970-10976.

Jones, E. W., Holliman, P. J., Connell, A., Davies, M. L., Baker, J., Hobbs, R. J., ... & Pleydell-Pearce, C. (2016). A novel dimethylformamide (DMF) free bar-cast method to deposit organolead perovskite thin films with improved stability. *Chemical communications*, *52*(23), 4301-4304.

Jones, T. W., Osherov, A., Alsari, M., Sponseller, M., Duck, B. C., Jung, Y. K., ... & Stranks, S. D. (2019). Lattice strain causes non-radiative losses in halide perovskites. *Energy & Environmental Science*, *12*(2), 596-606.

Joshi, S., Hasan, Z. I., Pruthvi, M., & Tulsiram, M. P. (2021). X-ray diffraction–A simplistic approach for perovskite based solar cells degradation studies. *Materials Today: Proceedings*, *35*, 31-34.

Jung, M., Ji, S. G., Kim, G., & Seok, S. I. (2019). Perovskite precursor solution chemistry: from fundamentals to photovoltaic applications. *Chemical Society Reviews*, *48*(7), 2011-2038.

Kabeyi, M. J. B. (2019). Geothermal electricity generation, challenges, opportunities and recommendations. *International Journal of Advances in Scientific Research and Engineering (ijasre)*, *5*(8), 53-95.

Ke, W., Zhao, D., Cimaroli, A. J., Grice, C. R., Qin, P., Liu, Q., ... & Fang, G. (2015). Effects of annealing temperature of tin oxide electron selective layers on the performance of perovskite solar cells. *Journal of Materials Chemistry A*, *3*(47), 24163-24168.

Krishnan, U., Kaur, M., Kumar, M., & Kumar, A. (2019). Factors affecting the stability of perovskite solar cells: a comprehensive review. *Journal of Photonics for Energy*, *9*(2), 021001-021001.

Ku, Z., Rong, Y., Xu, M., Liu, T., & Han, H. (2013). Full printable processed mesoscopic $CH_3NH_3PbI_3/TiO_2$ heterojunction solar cells with carbon counter electrode. *Scientific reports*, *3*(1), 3132.

Kuang, Y., Zardetto, V., Van Gils, R., Karwal, S., Koushik, D., Verheijen, M. A., ... & Creatore, M. (2018). Low-temperature plasma-assisted atomic-layer-deposited SnO2 as an electron transport layer in planar perovskite solar cells. *ACS applied materials & interfaces*, *10*(36), 30367-30378.

Kumar, A., & Gupta, U. (2021). Numerical assessment of high-efficiency lead-free perovskite solar cells. *Materials Today: Proceedings*, *45*, 5041-5046.

Kumar, A., Pandey, N., Punetha, D., Saha, R., Choudhary, S., & Chakrabarti, S. (2023, October). Reduced graphene oxide (rGO)-$CsSnI_3$ nanocomposites: a cost-effective technique to improve the structural and optical properties for optoelectronic device applications. In *Organic, Hybrid, and Perovskite Photovoltaics XXIV* (Vol. 12660, pp. 63-72). SPIE.

Kumar, M. H., Dharani, S., Leong, W. L., Boix, P. P., Prabhakar, R. R., Baikie, T., ... & Mathews, N. (2014). Lead-free halide perovskite solar cells with high photocurrents realized through vacancy modulation. *Advanced Materials (Deerfield Beach, Fla.)*, *26*(41), 7122-7127.

Kumar, N. S., & Naidu, K. C. B. (2021). A review on perovskite solar cells (PSCs), materials and applications. *Journal of Materiomics*, *7(5)*, 940-956.

Lauwerys, R. R., Kivits, A., Lhoir, M., Rigolet, P., Houbeau, D., Buchet, J. P., & Roels, H. A. (1980). Biological surveillance of workers exposed to dimethylformamide and the influence of skin protection on its percutaneous absorption. *International archives of occupational and environmental health*, *45*, 189-203.

Lee, Y. I., Jeon, N. J., Kim, B. J., Shim, H., Yang, T. Y., Seok, S. I., ... & Im, S. G. (2018). A low-temperature thin-film encapsulation for enhanced stability of a highly efficient perovskite solar cell. *Advanced Energy Materials*, *8*(9), 1701928.

Leijtens, T., Prasanna, R., Gold-Parker, A., Toney, M. F., & McGehee, M. D. (2017). Mechanism of tin oxidation and stabilization by lead substitution in tin halide perovskites. *ACS Energy Letters*, *2*(9), 2159-2165.

Li, B., Di, H., Chang, B., Yin, R., Fu, L., Zhang, Y. N., & Yin, L. (2021). Efficient passivation strategy on Sn related defects for high performance all-inorganic CsSnI3 perovskite solar cells. *Advanced Functional Materials*, *31*(11), 2007447.

Li, J., Munir, R., Fan, Y., Niu, T., Liu, Y., Zhong, Y., ... & Liu, S. F. (2018). Phase transition control for high-performance blade-coated perovskite solar cells. *Joule*, *2*(7), 1313-1330.

Liang, J., Liu, J., & Jin, Z. (2017). All-inorganic halide perovskites for optoelectronics: progress and prospects. *Solar Rrl*, *1*(10), 1700086.

Lin, L., Jones, T. W., Yang, T. C. J., Duffy, N. W., Li, J., Zhao, L., ... & Wilson, G. J. (2021). Inorganic electron transport materials in perovskite solar cells. *Advanced Functional Materials*, *31*(5), 2008300.

Lin, Y., Chen, B., Fang, Y., Zhao, J., Bao, C., Yu, Z., ... & Huang, J. (2018). Excess charge-carrier induced instability of hybrid perovskites. *Nature communications*, *9*(1), 4981.

Liu, M., Johnston, M. B., & Snaith, H. J. (2013). Efficient planar heterojunction perovskite solar cells by vapour deposition. *Nature*, *501*(7467), 395-398.

Liu, X., Wang, Y., Wu, T., He, X., Meng, X., Barbaud, J., ... & Han, L. (2020). Efficient and stable tin perovskite solar cells enabled by amorphous-polycrystalline structure. *Nature communications*, *11*(1), 2678.

López-Fraguas, E., Masi, S., & Mora-Sero, I. (2019). Optical characterization of lead-free Cs_2SnI_6 double perovskite fabricated from degraded and reconstructed $CsSnI_3$ films. *ACS applied energy materials*, *2*(12), 8381-8387.

Mali, S. S., Hong, C. K., Inamdar, A. I., Im, H., & Shim, S. E. (2017). Efficient planar nip type heterojunction flexible perovskite solar cells with sputtered TiO_2 electron transporting layers. *Nanoscale*, *9*(9), 3095-3104.

Marshall, K. P., Walker, M., Walton, R. I., & Hatton, R. A. (2017). Elucidating the role of the hole-extracting electrode on the stability and efficiency of inverted $CsSnI_3$/C60 perovskite photovoltaics. *Journal of Materials Chemistry A*, *5*(41), 21836-21845.

Marshall, K. P., Walton, R. I., & Hatton, R. A. (2015). Tin perovskite/fullerene planar layer photovoltaics: improving the efficiency and stability of lead-free devices. *Journal of materials chemistry A*, *3*(21), 11631-11640.

Mazumdar, S., Zhao, Y., & Zhang, X. (2021). Stability of perovskite solar cells: Degradation mechanisms and remedies. *Frontiers in Electronics*, *2*, 712785.

Mehde, M. S., Al-Gebori, A. M., & Hantoosh, A. K. (2020, March). The effect of the spinning speed variation on the perovskite solar cell efficiency. In *IOP Conference Series: Materials Science and Engineering* (Vol. 757, No. 1, p. 012071). IOP Publishing.

Mendhe, A. C. (2023). Spin coating: Easy technique for thin films. In *Simple Chemical Methods for Thin Film Deposition: Synthesis and Applications* (pp. 387-424). Singapore: Springer Nature Singapore.

Meng, F., Wang, D., Chang, J., Li, J., & Wang, G. (2024). Application of carbon materials in conductive electrodes for perovskite solar cells. *Solar RRL*, *8*(6), 2301030.

Misra, R. K., Aharon, S., Li, B., Mogilyansky, D., Visoly-Fisher, I., Etgar, L., & Katz, E. A. (2015). Temperature-and component-dependent degradation of perovskite photovoltaic materials under concentrated sunlight. *The journal of physical chemistry letters*, *6*(3), 326-330.

Mortadi, A., El Hafidi, E., Nasrellah, H., Monkade, M., & El Moznine, R. (2024). Analysis and optimization of lead-free perovskite solar cells: investigating performance and electrical characteristics. *Materials for Renewable and Sustainable Energy*, *13*(2), 219-232.

Nair, S., Patel, S. B., & Gohel, J. V. (2020). Recent trends in efficiency-stability improvement in perovskite solar cells. *Materials Today Energy*, *17*, 100449.

Nematov, D. D., Burkhonzoda, A. S., Kurboniyon, M. S., Zafari, U., Kholmurodov, K. T., Brik, M. G., ... & Shokir, F. (2025). The Effect of Phase Changes on Optoelectronic Properties of Lead-Free CsSnI3 Perovskites. *Journal of Electronic Materials*, 1-11.

Ng, C. H., Nishimura, K., Ito, N., Hamada, K., Hirotani, D., Wang, Z., ... & Hayase, S. (2019). Role of GeI_2 and SnF_2 additives for SnGe perovskite solar cells. *Nano Energy*, *58*, 130-137.

Nishimura, K., Kamarudin, M. A., Hirotani, D., Hamada, K., Shen, Q., Iikubo, S., ... & Hayase, S. (2020). Lead-free tin-halide perovskite solar cells with 13% efficiency. *Nano Energy*, *74*, 104858.

Nwanna, E. C., Imoisili, P. E., & Jen, T. C. (2022). Synthesis and characterization of SnO_2 thin films using metalorganic precursors. *Journal of King Saud University-Science*, *34*(5), 102123.

Olaleru, S. A., Kirui, J. K., Wamwangi, D., Roro, K. T., & Mwakikunga, B. J. S. E. (2020). Perovskite solar cells: The new epoch in photovoltaics. *Solar Energy*, *196*, 295-309.

Osman, M. M., Almutairi, Z., & Almuzaiqer, R. (2024). Effect of spin coating speeds on electrical and optical characteristic of perovskite $SrTiO_3$ thin films prepared by sol-gel method. *Results in Engineering*, *24*, 103046.

Parves, S., Mina, S., Nahid, F., Hussain, K. M. A., & Habib, A. (2020). Optical and structural properties of vacuum evaporated tin oxide (SnO2) thin films. *Research gate*.

Peters, I. M., & Buonassisi, T. (2018). Energy yield limits for single-junction solar cells. *Joule*, *2*(6), 1160-1170.

Qiu, X., Cao, B., Yuan, S., Chen, X., Qiu, Z., Jiang, Y., ... & Kanatzidis, M. G. (2017). From unstable $CsSnI_3$ to air-stable Cs_2SnI_6: A lead-free perovskite solar cell light absorber with band gap of 1.48 eV and high absorption coefficient. *Solar Energy Materials and Solar Cells*, *159*, 227-234.

Qu, Z., Zhao, Y., Ma, F., Mei, L., Chen, X. K., Zhou, H., ... & You, J. (2024). Enhanced charge carrier transport and defects mitigation of passivation layer for efficient perovskite solar cells. *Nature Communications*, *15*(1), 8620.

Roberts, A., Thomas, B., Sewell, P., Khan, Z., Balmain, S., & Gillman, J. (2016). Current tidal power technologies and their suitability for applications in coastal and marine areas. *Journal of Ocean Engineering and Marine Energy*, *2*, 227-245.

Roy, P., Sinha, N. K., Tiwari, S., & Khare, A. (2020). A review on perovskite solar cells: Evolution of architecture, fabrication techniques, commercialization issues and status. *Solar Energy*, *198*, 665-688.

Sabbah, H. (2022). Numerical simulation of 30% efficient lead-free perovskite $CsSnGeI_3$-based solar cells. *Materials*, *15*(9), 3229.

Samanta, A., Kumar, V., & Kanjilal, A. (2024). Exploring efficiency improvement by introducing Ge in CsSnI3 perovskite solar cells: computational approach. *Journal of Electronic Materials*, *53*(7), 4272-4286.

Sander, L., Jung, C., & Schindler, D. (2024). Global review on environmental impacts of onshore wind energy in the field of tension between human societies and natural systems. *Energies*, *17*(13), 3098.

Sathiyan, G., Wang, H., Chen, C., Miao, Y., Zhai, M., & Cheng, M. (2022). Impact of fluorine substitution in organic functional materials for perovskite solar cell. *Dyes and Pigments*, *198*, 110029.

Seyed-Talebi, S. M., & Beheshtian, J. (2021). Lead-free inorganic cesium tin-germanium triiodide perovskites for photovoltaic application. *International Journal of Energy and Power Engineering*, *15*(6), 252-257.

Shao, S., Dong, J., Duim, H., ten Brink, G. H., Blake, G. R., Portale, G., & Loi, M. A. (2019). Enhancing the crystallinity and perfecting the orientation of formamidinium tin iodide for highly efficient Sn-based perovskite solar cells. *Nano Energy*, *60*, 810-816.

Shao, S., Liu, J., Portale, G., Fang, H. H., Blake, G. R., ten Brink, G. H., ... & Loi, M. A. (2018). Highly reproducible Sn-based hybrid perovskite solar cells with 9% efficiency. *Advanced Energy Materials*, *8*(4), 1702019.

Sharenko, A., & Toney, M. F. (2016). Relationships between lead halide perovskite thin-film fabrication, morphology, and performance in solar cells. *Journal of the American Chemical Society*, *138*(2), 463-470.

Smith, D. (2024). The social impacts of dams and hydropower. In *Handbook of Social Impact Assessment and Management* (pp. 51-66). Edward Elgar Publishing.

Snaith, H. J., & Hacke, P. (2018). Enabling reliability assessments of pre-commercial perovskite photovoltaics with lessons learned from industrial standards. *Nature Energy*, *3*(6), 459-465.

Song, T. B., Yokoyama, T., Aramaki, S., & Kanatzidis, M. G. (2017). Performance enhancement of lead-free tin-based perovskite solar cells with reducing atmosphere-assisted dispersible additive. *ACS Energy Letters*, *2*(4), 897-903.

Song, T. B., Yokoyama, T., Stoumpos, C. C., Logsdon, J., Cao, D. H., Wasielewski, M. R., ... & Kanatzidis, M. G. (2017). Importance of reducing vapor atmosphere in the fabrication of tin-based perovskite solar cells. *Journal of the American Chemical Society*, *139*(2), 836-842.

Sönmezoğlu, S., Arslan, A., Serin, T., & Serin, N. (2011). The effects of film thickness on the optical properties of TiO_2–SnO_2 compound thin films. *Physica Scripta*, *84*(6), 065602.

Suazo, F. J. A., Shaji, S., Avellaneda, D. A., Aguilar-Martínez, J. A., & Krishnan, B. (2020). Solar cell using spray casted Cs_2SnI_6 perovskite thin films on chemical bath deposited CdS yielding high open circuit voltage. *Solar Energy*, *207*, 486-495.

Sutton, R. J., Filip, M. R., Haghighirad, A. A., Sakai, N., Wenger, B., Giustino, F., & Snaith, H. J. (2018). Cubic or orthorhombic? Revealing the crystal structure of metastable black-phase CsPbI3 by theory and experiment. *ACS Energy Letters*, *3*(8), 1787-1794.

Tomar, N., Agrawal, A., Dhaka, V. S., & Surolia, P. K. (2020). Ruthenium complexes-based dye sensitized solar cells: Fundamentals and research trends. *Solar Energy*, *207*, 59-76.

Tress, W., Marinova, N., Inganäs, O., Nazeeruddin, M. K., Zakeeruddin, S. M., & Graetzel, M. (2015). Predicting the open-circuit voltage of $CH_3NH_3PbI_3$ perovskite solar

cells using electroluminescence and photovoltaic quantum efficiency spectra: the role of radiative and non-radiative recombination. *Advanced Energy Materials*, *5*(3), 1400812.

Uddin, M. S., Al Mashud, M. A., Toki, G. I., Pandey, R., Zulfiqar, M., Saidani, O., ... & Hossain, M. K. (2024). Lead-free Ge-based perovskite solar cell incorporating TiO_2 and Cu_2O charge transport layers harnessing over 25% efficiency. *Journal of Optics*, *53*(4), 3726-3742.

Uysal, B. Ö., & Arıer, Ü. Ö. A. (2015). Structural and optical properties of SnO2 nano films by spin-coating method. *Applied Surface Science*, *350*, 74-78.

Vasconcelos, H. C., Meirelles, M., Özmenteş, R., & Korkut, A. (2024). Vacuum Ultraviolet Spectroscopic Analysis of Structural Phases in TiO2 Sol–Gel Thin Films. *Coatings*, *15*(1), 19.

Wan, J., Tao, L., Wang, Q., Zhang, K., Xie, J., Zhang, J., & Wang, H. (2021). A universal method for hysteresis-free and stable perovskite solar cells using water pre-treatment. *Chemical Engineering Journal*, *403*, 126435.

Wang, G., Chang, J., Bi, J., Lei, M., Wang, C., & Qiao, Q. (2022). Inorganic CsSnI3 perovskite solar cells: the progress and future prospects. *Solar RRL*, *6*(4), 2100841.

Wang, Q., Xiong, J., Xing, Y., Gan, X., Zhu, W., Xuan, R., ... & Zhang, J. (2024). Reductive Sn2+ Compensator for Efficient and Stable Sn-Pb Mixed Perovskite Solar Cells. *Advanced Science*, *11*(25), 2400962.

Wang, Y., Liu, X., Zhou, Z., Ru, P., Chen, H., Yang, X., & Han, L. (2019). Reliable measurement of perovskite solar cells. *Advanced Materials*, *31*(47), 1803231.

Wang, Y., Tong, A., Wang, Y., Liang, K., Zhu, W., Wu, Y., ... & Wu, J. (2024). Interfacial modulation by ammonium salts in hole transport layer free CsPbBr3 solar cells with fill factor over 86%. *Materials Today Chemistry*, *40*, 102228.

World Health Organization. Exposure to Lead: A Major Public Health Concern. 2010. Available online: https://www.who.int/publications/i/item/9789240037632 (accessed on 19 April 2023).

Wu, S., Li, Z., Li, M. Q., Diao, Y., Lin, F., Liu, T., ... & Jen, A. K. Y. (2020). 2D metal–organic framework for stable perovskite solar cells with minimized lead leakage. *Nature Nanotechnology*, *15*(11), 934-940.

Wu, T., Liu, X., Luo, X., Lin, X., Cui, D., Wang, Y., ... & Han, L. (2021). Lead-free tin perovskite solar cells. *Joule*, *5*(4), 863-886.

Xi, J., Wu, Z., Jiao, B., Dong, H., Ran, C., Piao, C., ... & Kanatzidis, M. G. (2017). Multichannel Interdiffusion Driven FASnI3 Film Formation Using Aqueous Hybrid Salt/Polymer Solutions toward Flexible Lead-Free Perovskite Solar Cells. *Advanced Materials*, *29*(23), 1606964.

Yan, Y., Zhou, P., Zhang, S. X., Guo, X. G., & Guo, D. M. (2018). Effect of substrate curvature on thickness distribution of polydimethylsiloxane thin film in spin coating process. *Chinese physics B*, *27*(6), 068104.

Yang, G., Chen, C., Yao, F., Chen, Z., Zhang, Q., Zheng, X., ... & Fang, G. (2018). Effective carrier-concentration tuning of SnO2 quantum dot electron-selective layers for high-performance planar perovskite solar cells. *Advanced Materials*, *30*(14), 1706023.

Yang, J., Siempelkamp, B. D., Liu, D., & Kelly, T. L. (2015). Investigation of $CH_3NH_3PbI_3$ degradation rates and mechanisms in controlled humidity environments using in situ techniques. *ACS nano*, *9*(2), 1955-1963.

Yu, Y., Hoang, M. T., Yang, Y., & Wang, H. (2023). Critical assessment of carbon pastes for carbon electrode-based perovskite solar cells. *Carbon*, *205*, 270-293.

Zeng, Q., Zhang, X., Liu, C., Feng, T., Chen, Z., Zhang, W., ... & Yang, B. (2019). Inorganic $CsPbI_2Br$ perovskite solar cells: the progress and perspective. *Solar Rrl*, *3*(1), 1800239.

Zhang, T., Guo, N., Li, G., Qian, X., Li, L., & Zhao, Y. (2016). A general non-CH_3NH_3X (X= I, Br) one-step deposition of $CH_3NH_3PbX_3$ perovskite for high performance solar cells. *Journal of Materials Chemistry A*, *4*(9), 3245-3248.

Zhang, W., Liu, H., Yan, F., Dong, B., & Wang, H. L. (2024). Recent Progress of Low-Toxicity Poor-Lead All-Inorganic Perovskite Solar Cells. *Small Methods*, *8*(2), 2300421.

Zhou, D., Zhou, T., Tian, Y., Zhu, X., & Tu, Y. (2018). Perovskite-based solar cells: materials, methods, and future perspectives. *Journal of Nanomaterials*, *2018*(1), 8148072.

Zhu, P., Chen, C., Gu, S., Lin, R., & Zhu, J. (2018). $CsSnI_3$ Solar Cells via an Evaporation-Assisted Solution Method. *Solar RRL*, *2*(4), 1700224.

Zuo, C., & Ding, L. (2015). Solution-Processed Cu_2O and CuO as Hole Transport Materials for Efficient Perovskite Solar Cells. *Small (Weinheim an der Bergstrasse, Germany)*, *11*(41), 5528-5532.

Zuo, F., Williams, S. T., Liang, P. W., Chueh, C. C., Liao, C. Y., & Jen, A. K. (2014). Binary-metal perovskites toward high-performance planar-heterojunction hybrid solar cells. *Advanced Materials (Deerfield Beach, Fla.)*, *26*(37), 6454-6460.

APPENDICES

Appendix I: Copy of research permit

REPUBLIC OF KENYA

NATIONAL COMMISSION FOR SCIENCE,TECHNOLOGY & INNOVATION

Ref No: **726896**

Date of Issue: **15/October/2024**

RESEARCH LICENSE

This is to Certify that Miss.. Marion Kerubo Kerubo of Egerton University, has been licensed to conduct research as per the provision of the Science, Technology and Innovation Act, 2013 (Rev.2014) in Kisii, Nairobi, Nakuru on the topic: Fabrication and Evaluation of Germanium doped Cesium Tin Triiodide Perovskite Solar Cells for the period ending : 15/October/2025.

License No: **NACOSTI/P/24/41216**

726896

Applicant Identification Number

Director General
NATIONAL COMMISSION FOR SCIENCE,TECHNOLOGY & INNOVATION

Appendix II: Abstract Page of Publication

International Journal of Physics, 2025, Vol. 13, No. 3, 62-68
Available online at http://pubs.sciepub.com/ijp/13/3/3
Published by Science and Education Publishing
DOI:10.12691/ijp-13-3-3

Optical, Structural and Morphological Characterization of Germanium Doped Cesium Tin Triiodide for Perovskite Solar Cells Applications

Marion Mogusu[1,*], Duke Oeba[1], Cliff Mosiori[2]

[1]Department of Physics, Faculty of Science, Egerton University, P.O. Box 536-20115, Egerton, Kenya
[2]Department of Mathematics and Physics, Technical University of Mombasa, P.O. Box 90420-80100, Mombasa, Kenya
*Corresponding author: mogusumarion@gmail.com

Received June 06, 2025; Revised July 08, 2025; Accepted July 15, 2025

Abstract In this work, germanium doped cesium tin triiodide ($CsSnI_3$-Ge) perovskite thin films, incorporated with a 5mole% germanium (Ge) concentration were deposited on fluorine doped tin (IV) oxide (FTO) substrates using spin coating technique and the films were synthesized under different spin coating speeds. Ge was used as a dopant to curb the problem of the rapid oxidation of tin (II) ions (Sn^{2+}) to tin (IV) ions (Sn^{4+}) in the presence of oxygen. Optical measurements were done using ultraviolet visible (UV-Vis) spectrophotometer, structural measurements were carried out using an X-ray diffraction (XRD) machine and the morphological analysis was done using a scanning electron microscope (SEM). The $CsSnI_3$-Ge layer deposited at a spin coating speed of 4000 revolutions per minute(rpm) displayed the highest absorbance with a band gap value in the range of 2.85 eV to 3.36 eV which was higher than the ideal value of ~1.5 eV. Structural analysis on the different $CsSnI_3$-Ge films displayed a consistent orthorhombic structure across all samples and SEM images revealed almost identical crystallite sizes. Generally, the perovskite film synthesized by spin coating speed of 4000 rpm displayed higher absorbance, higher crystallinity and a possibly uniform film morphology making it the optimal layer for solar cell applications.

Keywords: *Perovskites, tin oxidation, spin coating, thin films*

Cite This Article: Marion Mogusu, Duke Oeba, and Cliff Mosiori, "Optical, Structural and Morphological Characterization of Germanium Doped Cesium Tin Triiodide for Perovskite Solar Cells Applications." *International Journal of Physics*, vol. 13, no. 3 (2025): 62-68. doi: 10.12691/ijp-13-3-3.